



OPEN ACCESS

EDITED BY

Huizeng Liu,
Shenzhen University, China

REVIEWED BY

Zhigang Cao,
Chinese Academy of Sciences (CAS), China
Jamie Shutler,
University of Exeter, United Kingdom

*CORRESPONDENCE

Luis González Vilas
✉ luis.gonzalezvilas@artov.ismar.cnr.it

RECEIVED 11 July 2023

ACCEPTED 22 December 2023

PUBLISHED 16 January 2024

CITATION

González Vilas L, Brando VE, Di Cicco A, Colella S, D'Alimonte D, Kajiyama T, Attila J and Schroeder T (2024) Assessment of ocean color atmospheric correction methods and development of a regional ocean color operational dataset for the Baltic Sea based on Sentinel-3 OLCI.

Front. Mar. Sci. 10:1256990.

doi: 10.3389/fmars.2023.1256990

COPYRIGHT

© 2024 González Vilas, Brando, Di Cicco, Colella, D'Alimonte, Kajiyama, Attila and Schroeder. This is an open-access article distributed under the terms of the [Creative Commons Attribution License \(CC BY\)](https://creativecommons.org/licenses/by/4.0/). The use, distribution or reproduction in other forums is permitted, provided the original author(s) and the copyright owner(s) are credited and that the original publication in this journal is cited, in accordance with accepted academic practice. No use, distribution or reproduction is permitted which does not comply with these terms.

Assessment of ocean color atmospheric correction methods and development of a regional ocean color operational dataset for the Baltic Sea based on Sentinel-3 OLCI

Luis González Vilas^{1*}, Vittorio Ernesto Brando¹,
Annalisa Di Cicco¹, Simone Colella¹, Davide D'Alimonte²,
Tamito Kajiyama², Jenni Attila³ and Thomas Schroeder⁴

¹CNR-ISMAR, Istituto di Scienze Marine, Consiglio Nazionale delle Ricerche, Rome, Italy, ²AEQUORA LDA, Lisboa, Portugal, ³Finnish Environment Institute (SYKE), Helsinki, Finland, ⁴Commonwealth Scientific and Industrial Research Organization (CSIRO) Environment, Brisbane, QLD, Australia

The Baltic Sea is characterized by large gradients in salinity, high concentrations of colored dissolved organic matter, and a phytoplankton phenology with two seasonal blooms. Satellite retrievals of chlorophyll-*a* concentration (chl-*a*) are hindered by the optical complexity of this basin and the reduced performance of the atmospheric correction in its highly absorbing waters. Within the development of a regional ocean color operational processing chain for the Baltic Sea based on Sentinel-3 Ocean and Land Colour Instrument (OLCI) full-resolution data, the performance of four atmospheric correction processors for the retrieval of remote-sensing reflectance (*Rrs*) was analyzed. Assessments based on three Aerosol Robotic Network-Ocean Color (AERONET-OC) sites and shipborne hyperspectral radiometers show that POLYMER was the best-performing processor in the visible spectral range, also providing a better spatial coverage compared with the other processors. Hence, OLCI *Rrs* spectra retrieved with POLYMER were chosen as input for a bio-optical ensemble scheme that computes chl-*a* as a weighted sum of different regional multilayer perceptron neural nets. This study also evaluated the operational *Rrs* and chl-*a* datasets for the Baltic Sea based on OC-CCI v.6. The chl-*a* retrievals based on OC-CCI v.6 and OLCI *Rrs*, assessed against *in-situ* chl-*a* measurements, yielded similar results (OC-CCI v.6: $R^2 = 0.11$, bias = -0.22 ; OLCI: $R^2 = 0.16$, bias = -0.03) using a common set of match-ups for the same period. Finally, an overall good agreement was found between chl-*a* retrievals from OLCI and OC-CCI v.6 although differences between *Rrs* were amplified in terms of chl-*a* estimates.

KEYWORDS

ocean color, atmospheric correction, Baltic Sea, Sentinel-3 OLCI, chlorophyll-*a*, optically complex waters

1 Introduction

The Baltic Sea (Figure 1) is a brackish shallow semi-enclosed basin characterized by large inputs of pollutants and nutrients from natural and anthropogenic sources combined with a limited water exchange with the open ocean through the Danish Straits in the southwest, causing large latitudinal gradients of salinity and dissolved organic matter (Omstedt et al., 2004; Leppäranta and Myrberg, 2009). As a consequence of the strong anthropogenic pressure, pollution (HELCOM, 2018), eutrophication episodes (Andersen et al., 2011; Fleming-Lehtinen et al., 2015; Heiskanen et al., 2019), and/or phytoplankton blooms (Wasmund et al., 2011; Kahru et al., 2018; Hjerne et al., 2019) threaten its fragile ecosystems. Growing concern about the basin's health is raised by the Baltic Marine Environment Protection Commission (Helsinki Commission, HELCOM) (HELCOM, 2007). The Baltic Sea is characterized by high concentrations of colored dissolved organic matter (CDOM). Rivers are the main CDOM source, which follows a general dilution gradient from north to south with a large spatiotemporal variability driven by processes such as ice melting, rainfall, phytoplankton blooms, or photodegradation (Berthon and Zibordi, 2010; Ylöstalo et al., 2016; Simis et al., 2017; Kratzer and Moore, 2018).

Two seasonal phytoplankton blooms are usually observed in most areas of the Baltic Sea (Wasmund et al., 2011; Kahru et al., 2018; Brando et al., 2021). Firstly, a strong spring bloom dominated by

diatoms and dinoflagellates is responsible for most of the annual primary production in the area (Simis et al., 2017; Zhang et al., 2018). This spring bloom progresses from south to north due to light and nitrogen limitation, and it can cause anoxia and hypoxia events in the bottom layer because of the fast diatom sedimentation (Hjerne et al., 2019). After a minimum production in early summer (May–June), phosphorus excess and increasing surface water temperature lead to the blooming of nitrogen-fixing cyanobacteria, causing extensive and prolonged surface and near-surface accumulations of filamentous species during calm weather periods in July and August (Kahru et al., 1994; Finni et al., 2001; Kahru et al., 2007; Kahru et al., 2018).

Chlorophyll-*a* (chl-*a*) concentration (measured in mg m^{-3}) is one of the most relevant indicators for water quality monitoring within the Baltic Sea Action Plan implemented by HELCOM, as it is useful for assessing the eutrophication status and a good proxy for phytoplankton blooms (HELCOM, 2017; HELCOM, 2019; Ahlman et al., 2020). Compared with chl-*a* data from sampling stations, *in-situ* platforms, or automated ship measurements, chl-*a* maps derived from ocean color (OC) satellite images provide a synoptic view of the phytoplankton spatial distribution. Although data availability in terms of spatial coverage and temporal resolution is limited by the cloud cover, it can be significantly enhanced by merging data from different sensors (Groom et al., 2019; O'Reilly and Werdell, 2019; Sathyendranath et al., 2019).

Accuracy and reliability of chl-*a* retrievals from OC data depend on two related factors: 1) the optical characteristics of the

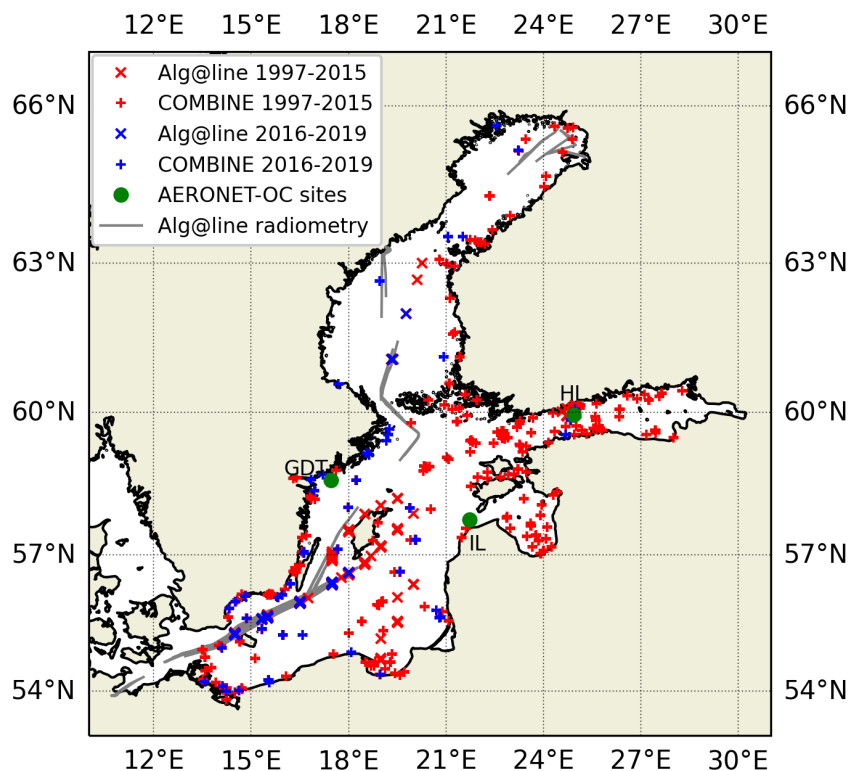


FIGURE 1

Study area showing the location of the *in-situ* measurements. The crosses identify the *in-situ* Alg@line chl-*a* data collected by the SYKE, whereas the pluses are chl-*a* data extracted from the COMBINE database (red points: 1997–2015; blue points: OLCI period from 2016 to 2019) (Section 2.2.2). The green dots mark the location of the AERONET-OC sites (GDT, Gustav Dalen Tower; HL, Helsinki Lighthouse; IL, Irbe Lighthouse; Section 2.2.1). Gray lines show the trajectories of the ships during the collection of the Alg@line shipborne radiometry data by SYKE in 2016 (Section 2.2.1).

water and 2) the performance of the atmospheric correction (AC) algorithms converting the spectral top-of-atmosphere (TOA) radiances measured by the satellite sensors to spectral remote-sensing reflectance (R_{rs} , defined as the ratio of the water-leaving radiance and the downwelling irradiance and measured in sr^{-1}) used as input in chl- a estimation algorithms (Brewin et al., 2015; Sathyendranath et al., 2019). Despite the good results in open-ocean and high-scattering coastal areas (Blondeau-Patissier et al., 2014; O'Reilly and Werdell, 2019), retrieval of reliable OC products from high-absorbing waters such as the Baltic Sea is a challenging task. High absorption coefficients related to the high CDOM concentrations (with aCDOM values exceeding 1.0 m^{-1} at 440 nm, Ylöstalo et al., 2016) in combination with relative low sun elevation lead to low R_{rs} values, especially in the blue part of the spectrum. Therefore, AC algorithms show a limited performance producing inaccurate R_{rs} spectra with low and even negative values (Attila et al., 2013; Beltrán-Abaunza et al., 2014; Alikas et al., 2020; Brando et al., 2021; Tilstone et al., 2022).

Regarding chl- a retrieval, standard blue-green band-ratio algorithms have been reported as not suitable for the Baltic Sea because they tend to a significant overestimation (Darecki and Stramski, 2004; Odermatt et al., 2012; D'Alimonte et al., 2016; Pitarch et al., 2016; Ligi et al., 2017; Kratzer and Moore, 2018). Better results have been achieved with regionalized blue-green ratios (Darecki and Stramski, 2004; Attila et al., 2013; Ligi et al., 2017), red-edge bands (Ligi et al., 2017), or neural network (NN) algorithms based on different sets of R_{rs} values (Kratzer and Vinterhav, 2010; Hieronymi et al., 2017; Toming et al., 2017; Kyryliuk and Kratzer, 2019), although accuracy is still hampered by the optical complexity of the basin and the low performance of the AC processors.

Within the Copernicus Marine Service (CMEMS, Le Traon et al., 2019; von Schuckmann et al., 2022), two operational chl- a data streams are available for the Baltic Sea based on OLCI and on merged multisensor time series. These data streams are based on sensor merging to improve the daily spatial coverage at 300 m and 1 km resolutions to support the operational oceanography users and environmental reporting needs (Le Traon et al., 2019; Sathyendranath et al., 2019; von Schuckmann et al., 2022).

Brando et al. (2021) proposed a new ensemble approach based on multilayer perceptron neural network (MLP) bio-optical algorithms (ENS-MLP), with results outperforming those based on other methods reported in the literature. This new approach was implemented in a fully reprocessed multisensor time series of R_{rs} and chl- a data at ~ 1 km spatial resolution (OCEANCOLOUR_BAL_BGC_L3_MY_009_133, 2023).

This work documents the implementation of the new R_{rs} and chl- a level-3 datasets for the Baltic Sea based on the complete Sentinel-3 A and B OLCI time series (2016 to present) of OC images at full resolution (300 m), using the same ENS-MLP approach for chl- a retrievals. To this aim, the following steps were carried out: 1) the selection of the best AC processor to obtain OLCI level-2 R_{rs} from level-1 data, 2) the assessment of the new OLCI level-3 R_{rs} dataset and comparison with the CMEMS multisensor dataset at 1 km resolution, and 3) the comparative validation analysis of the multisensor and OLCI level-3 chl- a datasets based on the ENS-MLP approach. The validation results were based on several *in-situ* data

sources: automated radiometry from the Aerosol Robotic Network-Ocean Color (AERONET-OC) sites in the Baltic Sea, shipborne hyperspectral radiometry collected by the Finnish Environment Institute (SYKE), and chl- a concentrations from Alg@line and COMBINE datasets.

The remainder of this document is structured as follows: Section 2 introduces the data and methods used in this work, describing the validation exercises; the results presented in Section 3 include a match-up summary, validation results for level-2 OLCI R_{rs} , level-3 R_{rs} and chl- a , and a comparison between CMEMS-OLCI level-3 and OC-CCI v.6 datasets. The discussion and concluding remarks are addressed in Sections 4 and 5, respectively.

2 Materials and methods

2.1 Satellite R_{rs}

2.1.1 Level-2 reflectance datasets

OLCI R_{rs} spectra were extracted from Sentinel-3 level-2 products processed by four different atmospheric correction algorithms: OLCI level-2 Water Full Resolution (WFR), POLYMER, Case 2 Regional CoastColour (C2RCC), and S3 FUB-CSIRO Coastal Water Processor (hereafter S3 FUB-CSIRO). All the level-2 products were derived from a set of Sentinel-3 level-1b Full Resolution (FR) images at 300 m resolution acquired over the Baltic Sea for both Sentinel-3A (between April 2016 and September 2022) and Sentinel-3B (between May 2018 and September 2022) missions.

The OLCI WFR products were available from the Ocean Colour baseline collection OL_L2M.003, processed by EUMETSAT using the OLCI L2 processor IPF-OL-2 version 07 (EUMETSAT, 2021; Zibordi et al., 2022). This product provides water-leaving reflectance data at the OLCI spectral bands between 400 nm and 1,020 nm except those bands dedicated to atmospheric measurements (Table 1). It also contains the pixel classification band Water Quality and Science Flags (WQSFs), providing information about invalid and/or suspicious pixels (Table 2).

POLYMER is a coupled ocean-atmosphere algorithm that applies polynomial functions to model the (TOA) spectral reflectance and sun glint, and it applies a forward bio-optical model for the water component. It was originally developed for MERIS from an atmospheric correction processor for case-1 waters that is able to deal with sun glint (Steinmetz et al., 2011; Steinmetz and Ramon, 2018). In this study, we applied POLYMERv.4.14 (<https://forum.hygeos.com/viewtopic.php?f=5&t=155>), which is already adapted to OLCI, providing fully normalized water-leaving reflectance data for 16 bands between 400 nm and 1,020.5 nm (Table 1), as well as a flag band (bitmask) with pixel classification (Table 2).

C2RCC applies parametrized radiative transfer models based on the successive order of scattering (SOS) technique to obtain a large database of simulated TOA radiances, which is then used as input to train a set of neural networks (NN) for the retrieval of water-leaving reflectance as well as other water products (Doerffer and Schiller, 2007; Brockmann et al., 2016). In this work, we applied C2RCC v.2 (<https://c2rcc.org/neural-nets/>), providing, among other outputs,

TABLE 1 Available wavelengths from OLCI level-2 (*: OLCI WFR, C2RCC, and POLYMER) and level-3 products, multisensor OC-CCI products, and AERONET-OC sites.

Satellite bands					AERONET-OC bands	
OLCI-level-2*	S3 FUB-CSIRO	CMEMS-OLCI	OC-CCI v.6	OC-CCI v4.2 (chl-a)	2005–2018	2018–2022
400		400				400
412.5	412.5	412.5	412	412	412*	412
442.5	442.5	442.5	443	443	443*	443
490	490	490	490	490	490*	490
510	510	510	510	510		510
					532	
560	560	560	560	555	551 ^{†1}	560
620	620	620				620
665	665	665	665	670	667*	667
673.75		673.75				
681.25		681.25				
708.75	708.75	708.75				
753.75						
778.75		778.75				779
865		865			870	865
885						
1,020.5					1,020	1,020

Bands available for validation during the OLCI period using data from AERONET-OC are shown in bold. Bands available for OC-CCI v.6 validation since 2005 until 2016 are indicated with the superscript † (*: 555 nm between 2005 and 2011).

TABLE 2 Flag bands and flag lists implemented for each AC processor.

AC	Flag band	Flag list
WFR	Wqsf	land, coastline, cloud ¹ , cloud_ambiguous ¹ , cloud_margin ¹ , invalid ² , cosmetic, saturated, suspect, hisolzen, highglint ⁴ , snow_ice, ac_fail, whitecaps, adjac, rwneg_o2 ⁵ , rwneg_o3 ⁵ , rwneg_o4 ⁵ , rwneg_o5 ⁵ , rwneg_o6 ⁵ , rwneg_o7 ⁵ , rwneg_o8 ⁵
C2RCC	c2rcc_flags	tosa_OOR, Rhow_OOR, Cloud_risk ¹
C2RCC S3 FUB-CSIRO	quality_flags	land, coastline, fresh_inland_water, bright ³ , straylight_risk, invalid ² , cosmetic, sun_glint_risk ⁴ , dubious, saturated_OaXX (with XX from 01 to 21).
POLYMER	Bitmask	land, cloud_base ¹ , l1_invalid ² , negative_bb, out_of_bounds ⁶ , exception, thick_aerosol ⁶ , high_air_mass ⁶ , external_mass, inconsistency ⁶ , anomaly_rwmod_blue ⁶
IdePix	pixel_classif_flags	land, coastline, invalid ² , cloud ¹ , cloud_buffer ¹ , cloud_shadow ¹ , snow_ice, bright ³ , white, mountain_shadow

IdePix was used for all the AC processors as a common flag framework. Subscript numbers indicate the flag lists used for the outputs in Figure 3 (¹CLOUD; ²INVALID; ³BRIGHT; ⁴SUNGLINT_RISK; ⁵RNEG; ⁶POLYMER).

Rrs data for 16 OLCI bands between 400 nm and 1,020.5 nm (Table 1) and two flag bands (c2rcc_flag and quality_flags) with pixel identification information (Table 2).

The S3 FUB-CSIRO Coastal Water Processor is an ensemble neural network inversion trained with extensive coupled ocean-atmosphere radiative transfer simulations (Schroeder et al., 2022). The algorithm was adapted to an approach previously developed by Schroeder et al. (2007); Schroeder et al. (2003) for MERIS. The S3 FUB-CSIRO processor version 1.0.0.0.5.3 used in this study, therefore, does not provide outputs for OLCI bands at 400 nm, 673.75 nm, 681.25 nm, and above 708.75 nm (Table 1). The algorithm performs a pixel-per-pixel direct inversion of the TOA radiance signal into spectral remote sensing reflectance at mean sea level and selected water quality parameters. It also provides per-pixel sensor and inverse model uncertainties, which were not further evaluated in this study. Quality control was applied by using the flag band quality_flags for masking (Table 2), which are based on the level-1b flags but not the additional neural network-specific input/output out-of-range flags.

2.1.2 Level-3 reflectance datasets

Within CMEMS, two operational ocean color time series are available for the Baltic Sea: merged OLCI (Sentinel-3A and

Sentinel-3B) at 300 m spatial resolution and merged multisensor at 1 km resolution.

The CMEMS-OLCI level-3 *Rrs* dataset for the Baltic Sea merges OLCI level-2 *Rrs* spectra retrieved from level-1b FR images for both Sentinel-3A and Sentinel-3B missions using POLYMERv.4.14. *Rrs* values are remapped using the “nearest value” interpolation on an equi-rectangular grid at 300 m resolution. As in the EUMETSAT v.3.0.1 reprocessing the System Vicarious Calibration gains that have been implemented by EUMETSAT for both sensors, *Rrs* values are merged without any bias correction. The dataset has been produced operationally by CNR as daily data since April 2016 to present for 11 OLCI bands between 400 nm and 708.74 nm (Table 1) and is available at the Copernicus Marine Service in near real-time (OCEANCOLOUR_BAL_BGC_L3_NRT_009_131, Baltic Sea Ocean Colour Plankton, Reflectances, Transparency and Optics L3 NRT daily observations, 2023) and as a fully reprocessed multiyear time series (OCEANCOLOUR_BAL_BGC_L3_MY_009_133, 2023).

The CMEMS multisensor level-3 *Rrs* dataset for the Baltic Sea is derived from the Ocean Color (OC)-Climate Change Initiative (CCI) v.6 processor (OC-CCI v.6) implemented by Plymouth Marine Laboratory (PML) (Sathyendranath et al., 2019; OC-CCI, 2022; Sathyendranath et al., 2022). Data were obtained from different sensors and processed with specific atmospheric correction algorithms to obtain L2 *Rrs* spectra: NASA standard atmospheric correction was applied to the SeaWiFS NASA R2018.0 reprocessed dataset, while POLYMER was selected for MERIS (ESA 4th reprocessing) MODIS-AQUA and VIIRS (NASA R2018.0, included only until the end of 2019) and both OLCI sensors (EUMETSAT v.3.0.1 reprocessing). *Rrs* output values from each sensor were band-shifted using the inverse and direct application of the Quasi-Analytical Algorithm (QAA) algorithm (Lee et al., 2014; Mélin and Sclép, 2015) to six MERIS bands (Table 1) and then bias-corrected and merged at 1 km resolution, providing a consistent time series from 1997 to 2022.

2.2 *In situ* data for validation

2.2.1 *In situ* automated radiometry

For the validation of satellite-derived *Rrs*, this study relies on two sources of *in-situ* automated above-water radiometry: the AERONET-OC and the Alg@line hyperspectral datasets were collected following the same above-water radiometry approach (Zibordi et al., 2009; Simis and Olsson, 2013).

In-situ radiometry data were available from the automated measurements collected by AERONET-OC at three sites in the Baltic Sea: Gustav Dalen Tower (58.594°N, 17.467°E), with data from 2005 to 2022; Helsinki Lighthouse (59°949°N, 24.925°E), from 2006 to 2019; and Irbe Lighthouse (57.751°N, 21.723°E), from 2018 to 2022. Due to the illumination conditions of the Baltic Sea, data are usually available between May and September, with some single days in March, April, or October. We used level-2 data available from the AERONET-OC web page (<https://aeronet.gsfc.nasa.gov>), consisting of quality-controlled measurements of normalized water-leaving radiances (L_{wN}) corrected for bidirectional effects and referred to nadir (Zibordi et al., 2009; Zibordi et al., 2020). AERONET-OC

provides multispectral data (Table 1): 8 bands between 412 nm and 1,020 nm until 2018 (adapted to MERIS) and 11 bands between 400 nm and 1,020 nm since 2019 when instruments were modified for OLCI validation (Zibordi et al., 2009, 2020).

The Alg@line hyperspectral dataset was collected by SYKE within the BONUS FerryScope project (Simis and Olsson, 2013; Simis et al., 2021) from April to September 2016. Data were acquired every 15 s using a three-spectroradiometer system mounted approximately 7 m from the sea surface on board the merchant vessels Finnmaid (Finnlines) and Transpaper (Transatlantic). Downwelling irradiance (E_d) was collected using a TriOS RAMSES-ACC unit with a cosine collector, and sky (L_d) and water radiance (L_s) were measured with RAMSES-ARC sensors with a 7° field of view. The dataset was filtered to eliminate measurements with an obstructed view of the sea or affected by underexposure or oversaturation. *Rrs* spectra were derived by correcting for the reflection of sky radiance at the water surface using E_d , L_d , and L_s measurements. More details about data collection, processing, and quality control are available from Simis et al. (2021); Qin et al. (2017), and Warren et al. (2019).

2.2.2 *In situ* chl-*a* datasets

We used two *in-situ* datasets in order to validate the chl-*a* concentrations retrieved from satellite *Rrs* for the Baltic Sea: Alg@line and COMBINE.

The Alg@line dataset is derived from a set of water samples collected by SYKE from 1997 to 2017 using an acquisition system installed on board ferries operating in the Helsinki-Travemünde, Helsinki-Stockholm, and Kemi-Travemünde transects. Water samples (from surface to 5 m depth) were filtered using glass fiber filters (Whatman GF/F, 0.7- μ m nominal pore size), chlorophyll-*a* was extracted with ethanol, and concentrations were determined by fluorometry using a Jasco FP-750 spectrofluorometer or a Perkin-Elmer LS2-b fluorometer with an excitation wavelength of 413 nm and emission wavelength of 668 nm (Fleming and Kaitala, 2006; Kaitala et al., 2008).

The COMBINE dataset, available from the International Council for the Exploration of the Sea (ICES) oceanographic database, includes chl-*a* measurements gathered by several institutions from the 1970s to the present within the HELCOM marine monitoring program (HELCOM, 2017; HELCOM, 2019). Chl-*a* concentrations were obtained using different analytical protocols and techniques, from fluorimetry to spectrophotometry and HPLC, but always meeting the quality requirements established by the program. We excluded from the analysis data acquired in the Skagerrak and Kattegat regions since these basins are characterized by physical and optical water properties deemed different from the actual Baltic Sea (Ligi et al., 2017; Simis et al., 2017).

2.3 Chl-*a* retrieval algorithm from satellite *Rrs*

Retrieval of chl-*a* concentrations from satellite *Rrs* in the Baltic Sea was based on the methodological approach proposed by Brando et al. (2021). It builds on a bio-optical ensemble scheme in which chl-*a* concentrations are estimated as a weighted sum of the outputs

of different regional multilayer perceptron neural net (MLP) bio-optical algorithms developed using *in-situ* data available from the JRC/EC BiOMaP program (D'Alimonte et al., 2011; Zibordi et al., 2011). Weights defining the contribution of each individual MLP algorithm are dynamically established through the novelty index (D'Alimonte et al., 2014; Kajiyama et al., 2019; Brando et al., 2021).

Each MLP bio-optical algorithm uses as input *Rrs* values at a different subset of wavelengths, considering all the SeaWiFS bands implemented in the OC-CCI v4.2 product (Table 1): *chl-aMLP6b* (*Rrs* values at 412, 443, 490, 510, 555, and 670 nm), *chl-aMLP_5b* (*Rrs* values at 443, 490, 510, 555, and 670 nm), *chl-aMLP_4b* (*Rrs* values at 490, 510, 555, and 670 nm), and *chl-aMLP_3b* (*Rrs* values at 490, 510, and 555 nm).

Brando et al. (2021) tested two ensemble solutions based on four (*chl-aENS4*: *chl-aMLP_6b*, *chl-aMLP_5b*, *chl-aMLP_4b*, *chl-aMLP_3b*) and three (*chl-aENS3*: *chl-aMLP_5b*, *chl-aMLP_4b*, *chl-aMLP_3b*) MLP algorithms, evaluating their performance through a match-up analysis of *chl-a* retrievals from OC-CCI v4.2 time series against *in-situ* *chl-a* concentrations. Results showed that both ensemble solutions outperformed all the band-ratio regression algorithms based on *Rrs* spectral slopes instead of *Rrs* values at different bands and that *chl-aENS3* outperformed *chl-aENS4*.

In this work, the performance of both *chl-aENS3* and *chl-aENS4* was evaluated through a match-up analysis of *chl-a* retrievals from satellite *Rrs* extracted from the CMEMS-OLCI level-3 *Rrs* dataset and OC-CCI v.6 datasets (see Section 2.1.2), against *in-situ* *chl-a* measurements from Alg@Line and COMBINE datasets (see Section 2.2.2). Only results for the best-performing solution, i.e., *chl-aENS3*, are shown in this document.

Chl-aENS3 was also the selected algorithm for the implementation of the new CMEMS-OLCI level-3 *chl-a* dataset for the Baltic Sea (OCEANCOLOUR_BAL_BGC_L3_MY_009_133, 2023; OCEANCOLOUR_BAL_BGC_L3_NRT_009_131, 2023), in which *chl-a* concentrations are retrieved from the CMEMS-OLCI level-3 *Rrs* dataset merging *Rrs* outputs from POLYMERv.4.14 (see Section 2.2.1). The new dataset was produced by CNR for the complete OLCI time series (from April 2016 to the present).

As *chl-aENS3* was developed considering the SeaWiFS spectral bands available in the OC-CCI v4.2 product, in this work, *chl-a* retrievals using *Rrs* values from CMEMS-OLCI or OC-CCI v.6 required a previous band shift to the SeaWiFS spectral bands. The band shift was performed through the inverse and direct application of the QAA algorithm (Mélin and Sclep, 2015; Lee et al., 2009) modified to ensure non-negative phytoplankton at any band (Brando et al., 2021).

2.4 Validation exercises

2.4.1 Workflow

Figure 2 summarizes the workflow for the validation exercises carried out in this work, all of them implemented using a Match-up Database File (MDB) infrastructure (EUMETSAT, 2019; González Vilas et al., submitted; González Vilas et al., 2023).

The top panel (Figure 2A) depicts the steps for a round-robin comparison of four AC algorithms (i.e., WFR, C2RCC, POLYMER,

and S3 FUB-CSIRO) to select the best processor for deriving OLCI level-2 *Rrs* spectra from level-1 data. *In-situ* radiometry data for this comparative validation exercise were available from both the AERONET-OC and Alg@line hyperspectral datasets. The bottom panel of Figure 2B shows the validation procedure for the *Rrs* and *chl-a* level-3 datasets, comparing the new CMEMS-OLCI and OC-CCI v.6 datasets. In this case, only radiometric data from AERONET-OC were used for *Rrs* validation.

We also run the Identification of Pixels Properties (IdePix) to obtain a common flag band for all the processors. IdePix is a multisensor pixel identification tool available as a plugin for Sentinel Application Platform (SNAP) implementing pixel identification algorithms for different sensors including Sentinel-3 (<https://www.brockmann-consult.de/portfolio/idepix/>). It classifies pixels certainly or ambiguously affected by clouds and provides also other flags as *white* or *bright* (Table 2).

The main steps are the following ones (note that some steps are common for both analyses):

- Trimming: With the aim of reducing the AC computational time, level-1b FR images were first trimmed into microgranules keeping the OLCI data format (SENTINEL-SAFE). In the case of AERONET-OC or *chl-a* measurements, microgranules cover an area of 2° by 2° around the site location. For shipborne radiometry, granules were trimmed to cover the daily transect. The same protocol was also adopted for trimming the level-2 WFR and level-3 files.
- Atmospheric correction (Figure 2A): POLYMER, C2RCC, S3 FUB-CSIRO, and IdePix were run on the level-1b microgranules using default options. POLYMER is available from the HYGEOS website, and it is run directly in Python. C2RCC and IdePix are available as SNAP, while the S3 FUB-CSIRO processor is available as a Python/C plugin for SNAP at <https://github.com/s3tbx-fub-csiro/s3tbx-fub-csiro.git>. C2RCC, IdePix, and S3 FUB-CSIRO were processed using the SNAP Graph Processing Tool (GPT).
- Chl-a* processing (Figure 2B): Satellite *chl-a* was retrieved from level-3 microgranules using the method proposed by Brando et al. (2021) (Section 2.3).
- Generation of satellite extract files: Level-2 extract files (Figure 2A) were created for the Sentinel-3A or Sentinel-3B mission and each AC processor (WFR, POLYMER, C2RCC, and S3 FUB-CSIRO) starting from the corresponding output microfiles. Each extract file contains 25 × 25 pixels of satellite data centered at the site location (for AERONET-OC) or transect point(s) (for shipborne radiometry). These files include always *Rrs* for all the available bands, geometry (zenith and azimuth observation and sun angles), the flag band corresponding to the processor (see Section 2.1.1), and the IdePix results. If output values are defined as water-leaving reflectance (WFR and POLYMER), they are converted to *Rrs* by dividing by pi. The satellite overpass time and band wavelengths are also included in the files.

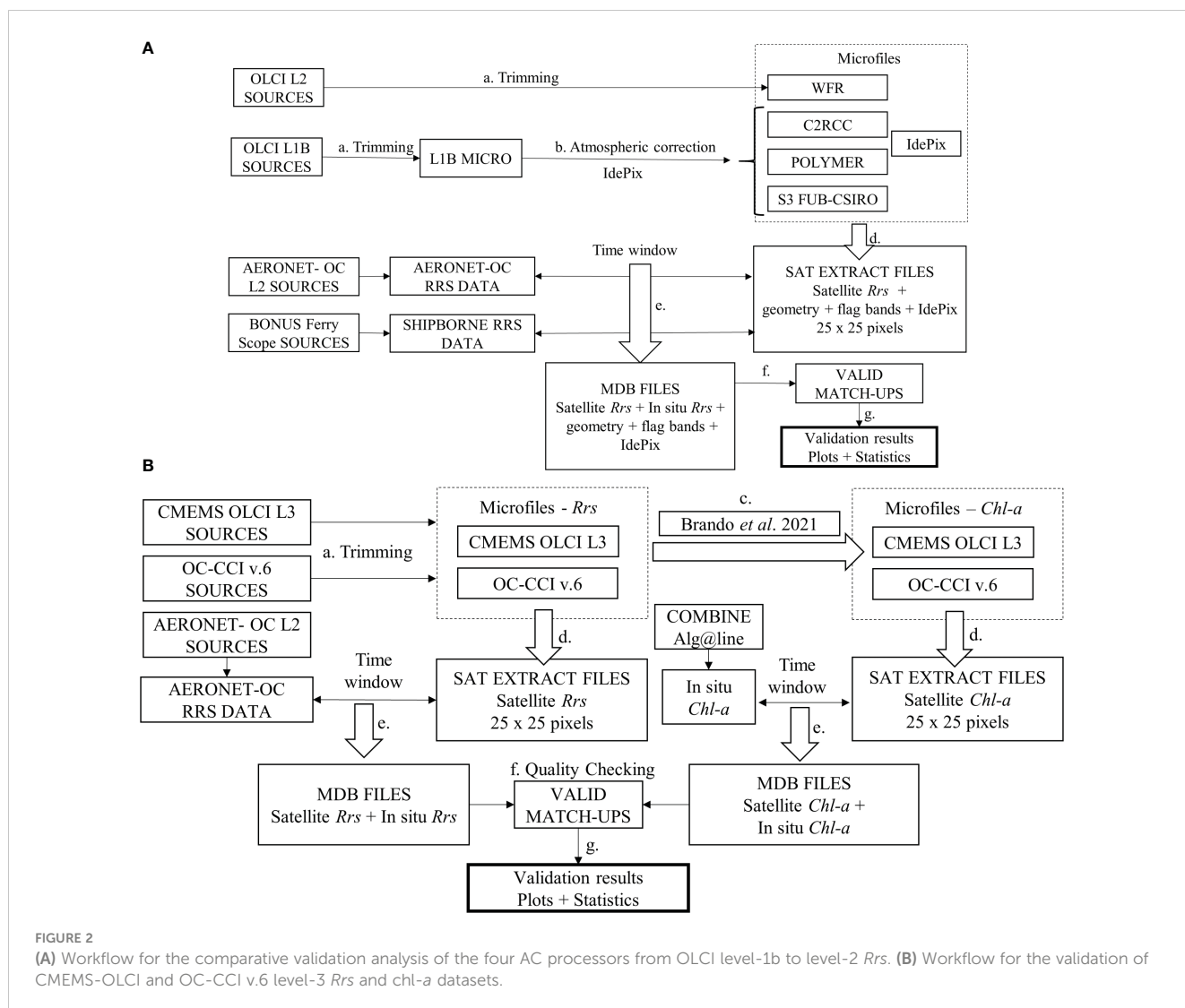


FIGURE 2

(A) Workflow for the comparative validation analysis of the four AC processors from OLCI level-1b to level-2 *Rrs*. (B) Workflow for the validation of CMEMS-OLCI and OC-CCI v.6 level-3 *Rrs* and *chl-a* datasets.

In the case of shipborne radiometry, to reduce the number of extracts associated with a single satellite image, extract files were only created if the time difference between the satellite overpass and the transect points within a given central pixel was lower than 15 min.

Level-3 extract files (Figure 2B) produced from level-3 microfiles include a window of 25×25 pixels of *Rrs* for all the bands around the AERONET-OC site or *chl-a* concentrations around the measurement location. Unlike level-2 extract files, flag bands are not required since invalid pixels were already masked in the source datasets during the level-3 creation. Moreover, as data with different acquisition times and observation geometries are merged, satellite time is limited to the date, and geometry information is not available.

e) Generation of MDB files: An MDB file is created as a NetCDF file including all the potential match-ups, i.e., spatiotemporal collocations between satellite and *in-situ* data, in this case, *Rrs* spectra or *chl-a* concentrations. MDB files are built by associating the satellite data from each extract file with the corresponding *in-situ* spectra or *chl-a*

measurements. For level-3 extracts merging sensors with different acquisition times, satellite time is set to 9:30 UCT, which is approximately the average overpass time in the Baltic Sea considering all the sensors (Brando et al., 2021). By default, the maximum time difference between satellite and *in-situ* acquisitions is set to 3 h for AERONET-OC and *chl-a* measurements and 15 min for shipborne radiometry (see Section 2.4.3). Normalized water-leaving radiances available in the AERONET-OC level-2 source files (see Section 2.2.1) were transformed to *Rrs* by dividing by the extra-solar irradiance spectrum and then band-shifted to the OLCI or OC-CCI v.6 spectral wavelengths using inverse and direct application of the QAA algorithm (Mélain and Sclep, 2015; Lee et al., 2009). Shipborne radiometry data (already available as *Rrs*) and *chl-a* concentrations (in mg m^{-3}) were incorporated directly into the MDB files.

f) Quality checking: Starting from the MDB file with all the potential match-ups, we applied the quality control protocols to obtain valid match-ups for the statistical analysis (details are provided in Sections 2.4.2 and 2.4.3).

- g) Statistical analysis: Plot generation and computation of validation metrics (see Section 2.4.4) using the valid match-ups.

2.4.2 Satellite quality control

Satellite quality control was based on the recommendations for OLCI or other medium-resolution satellites (Concha et al., 2021; Cazzaniga et al., 2022; Zibordi et al., 2022).

In this study, we used extraction windows of 3×3 pixels centered on the site only with 100% of valid pixels (9 pixels). Satellite *Rrs* for each band or *chl-a* concentrations were computed as the mean excluding outliers, considering a single pixel as an outlier if out of the range defined as the mean ± 1.5 standard deviations (EUMETSAT, 2022).

Pixels were masked according to two flag bands: IdePix and the specific flag band for each atmospheric correction algorithm. IdePix is used as a common framework for obtaining a set of common match-ups, whereas the specific flag band is useful for evaluating the spatial coverage of each AC processor in case of being applied operationally. Flag lists are summarized in Table 2.

Geometry was also considered for validation of level-2 *Rrs*, masking pixels with an observation zenith angle greater than 60° and a sun zenith angle greater than 70° .

We applied a spatial homogeneity test for *Rrs* validation by excluding match-ups with a coefficient variation (CV) at 560 nm higher than 20%. Note that CV is computed after the removal of out-of-range pixels (defined as the mean ± 1.5 standard deviations).

2.4.3 In situ quality control

As AERONET-OC systems acquire spectral measurements several times per day (usually every 20 min), MDB files can include up to 30 *in-situ* valid spectra for each satellite acquisition within the default 3-h time window. The validation was based on the closest spectrum in time with respect to the satellite overpass with a maximum time difference of 2 h.

For the Alg@line hyperspectral shipborne radiometry, the number of spectra in the central pixel within the 15-min time window varies from 1 to 3. Validation was also based on the closest spectrum in time.

In the case of *chl-a*, measurements collected between 7:00 UTC and 16 UTC on the same day as the satellite overpass were considered for obtaining valid match-ups.

2.4.4 Validation metrics

As validation metrics, we used the determination coefficient (R^2), the absolute percent differences (APD), the root mean square deviation (RMSD), the relative percent differences (RPD), and the bias parameter between the *in-situ* (x) and satellite measurements (expected y):

$$R^2 = \frac{\sum_{i=1}^N (x_i - \bar{x})(y_i - \bar{y})}{\sqrt{\sum_{i=1}^N (x_i - \bar{x})^2} \sqrt{\sum_{i=1}^N (y_i - \bar{y})^2}}$$

$$RMSD = \sqrt{\frac{\sum_{i=1}^N (y_i - x_i)^2}{N}}$$

$$APD = \frac{1}{N} \sum_{i=1}^N \frac{|y_i - x_i|}{x_i} \times 100 \%$$

$$RPD = \frac{1}{N} \sum_{i=1}^N \frac{y_i - x_i}{x_i} \times 100 \%$$

$$bias = \frac{1}{N} \sum_{i=1}^N y_i - x_i$$

The determination coefficient R^2 (unitless) assesses the agreement between both variables ranging from 0 (no agreement) to 1 (perfect agreement). The bias (in *Rrs* units: sr^{-1} , or *chl-a* units: $mg\ m^{-3}$) is useful for determining if there is overestimation (positive values) or underestimation (negative values). RMSD and APD (%) measure the absolute error in absolute units or percentage, respectively. Likewise, RPD (%) is a measurement of the relative error, but measured in percentage. In the case of *chl-a*, R^2 , RMSD, and bias are computed on log-transformed data, whereas RPD and APD are based on non-transformed values. As error measurement, APD is preferred for the *chl-a* because RMSD is more difficult to interpret since it is based on log-transformed data, where RMSD is used for *Rrs* validation.

2.5 Comparison between CMEMS-OLCI level-3 and OC-CCI v.6 datasets

As within CMEMS two operational *Rrs* and *chl-a* datasets are available for the Baltic Sea, the consistency of the times series with spatial resolutions at 300 m and 1 km was assessed. To this aim, the CMEMS-OLCI level-3 and multisensor datasets were compared through the extraction of a set of co-located data points. Values were extracted from an image every 10 days from 1 May 2016 to 31 December 2022. These daily images were sampled based on a regular grid of $10\ km \times 10\ km$ (115×119 longitude–latitude points), using the corresponding pixel value for the multisensor 1-km dataset and the mean on a 3×3 window for OLCI (only cases with 9 valid values were considered). The extraction was carried out for the five *Rrs* bands involved in the *chl-a* retrieval (i.e., 443 nm, 490 nm, 510 nm, 555 nm, and 670 nm) and for the *chl-a* concentration itself. Then, we obtained the scatter plots and computed the validation metrics (Section 2.4.4).

3 Results

3.1 Match-up summary and flagging analysis

Table 3 shows the number of total and valid match-ups available for the validation of level-2 (OLCI) and level-3

TABLE 3 Total and valid number of match-ups available for *Rrs* validation of OLCI level-2 and level-3 (CMEMS-OLCI and OC-CCI v.6) datasets.

		OLCI level 2						Level 3				
		All	Valid				C.M.	CMEMS-OLCI		OC-CCI v.6		C.M.
			WFR	C2RCC	POL.	S3 FUB-CSIRO		All	Valid	All	Valid	
AERONET	Total	1,161	546	522	773	538	392	706	486	785	561	433
	GDL	564	292	274	404	285	215	338	241	377	266	210
	HLH	185	79	80	117	84	53	141	90	164	122	80
	ILH	412	175	168	252	169	124	227	155	244	173	143
SYKE		348	182	114	207	117	110					

AERONET-OC sites are Gustav Dalen Tower (GDL), Helsinki Lighthouse (HLH), and Irbe Lighthouse (ILH). C.M. indicates the number of common match-ups for both level-2 and level-3 datasets; POL.: POLYMER v.4.14.

(CMEMS-OLCI and OC-CCI v.6) *Rrs* datasets, using both AERONET-OC and SYKE data.

When considering *in-situ* data from AERONET-OC sites, POLYMER is able to generate a higher number of valid match-ups for OLCI level-2 *Rrs* validation as compared with other AC processors (~65% of valid match-ups against ~45%), which show comparable figures. The percentage of valid match-ups is lower using SYKE data, but with a similar pattern: POLYMER shows the highest validity rate (~60%), followed by WFR (~52%) and finally C2RCC and S3 FUB-CSIRO (~35%).

Regarding the level-3 *Rrs* validation, both CMEMS-OLCI and OC-CCI v.6 show similar numbers with percentages of valid match-ups of approximately 70%, as expected considering that both datasets are mainly based on POLYMER.

As for the distribution across the AERONET-OC sites, the number of total (and valid) match-ups reveals the data availability, with more match-ups from Gustav Dalen Tower (data from 2016 to 2022), followed by Irbe Lighthouse (data from 2018 to 2022) and finally Helsinki Lighthouse (data from 2016, 2017, and 2019). Temporally, the number of match-ups has increased since 2018 (e.g., from 45 POLYMER valid match-ups in 2017 to 98 in 2018) with the launch of Sentinel-3B, being 2019 the year with the highest number as *in-situ* spectra were available from the three sites (e.g., 202 valid match-ups using POLYMER). The number of match-ups was also smaller in 2020 because the instruments were operational for a limited period (mainly between July and August) due to the COVID restrictions (56 valid POLYMER match-ups against 150 in 2021 or 171 in 2022).

Validation results shown in the following sections are based on common match-ups, i.e., those valid for all the AC processors in the case of level-2 *Rrs* validation and for both datasets (OLCI and OC-CCI v.6) in the case of level-3 *Rrs* validation.

Figure 3 shows a summary of the potential match-ups classified as invalid because at least one pixel in the 3×3 extraction window over the AERONET-OC sites was flagged using IdePix and/or other specific flag bands (Table 2).

The number of match-ups affected by cloud cover varies from 150 to almost 300 match-ups, depending on the flag band specific to each processor (Table 2). As *in-situ* data and potential match-ups

are mainly available from April to September, cloud coverage percentage is relatively low (between 10% and 30%) when compared with sites located in mid-latitudes.

Sun glint risk was the most frequent flag based on *quality_flags* (C2RCC and S3 FUB-CSIRO) with more than 330 match-ups, although this number is limited to only 87 match-ups using *wqsf* (WFR).

A common problem in the CDOM-dominated Baltic Sea waters affecting more than 230 potential match-ups is the negative reflectance retrievals (RNEGs), mainly in the blue part of the spectrum, i.e., *rneg_02* (412 nm) and *rneg_03* (443 nm). Note that *rneg_* flags included in *wqsf* (WFR) allow negative values up to a threshold (EUMETSAT, 2021) so that some valid match-ups could include slightly negative reflectance values.

A remarkable number of match-ups were also flagged as *invalid* (42 match-ups in all the flag bands) and *bright* (133 match-ups using IdePix and *quality_flags*). Other flags (not shown in Figure 3) were identified in a small number of match-ups (less than 5), including the *suspect*, *dubious*, *whitecaps*, or *ac_fail* cases.

Approximately 100 match-ups were flagged by one of the flags in POLYMER *bitmask* (*out_of_bounds*, *thick_aerosol*, *high_air_mass*, *external_mass*, *inconsistency*, *anomaly_rwmod_blue*), joining to the match-ups classified as cloud (*cloud_base*) or invalid (*ll_invalid*). However, approximately 74 match-ups flagged as SUNGLINT_RISK or 146 as RNEG are considered valid using *bitmask* or IdePix, explaining the higher number of valid POLYMER match-ups as compared with other AC processors.

3.2 Level-2 *Rrs* validation

This section reports the validation results for OLCI level-2 *Rrs* processed using the four AC processors: WFR (standard AC), C2RCC, POLYMER, and S3 FUB-CSIRO (see Section 2.1.1). Satellite *Rrs* were validated against *in-situ* radiometric data from AERONET-OC (Section 3.2.1) and Alg@line shipborne radiometry (Section 3.2.2) based on common sets of 392 and 100 valid match-ups, respectively (Table 3).

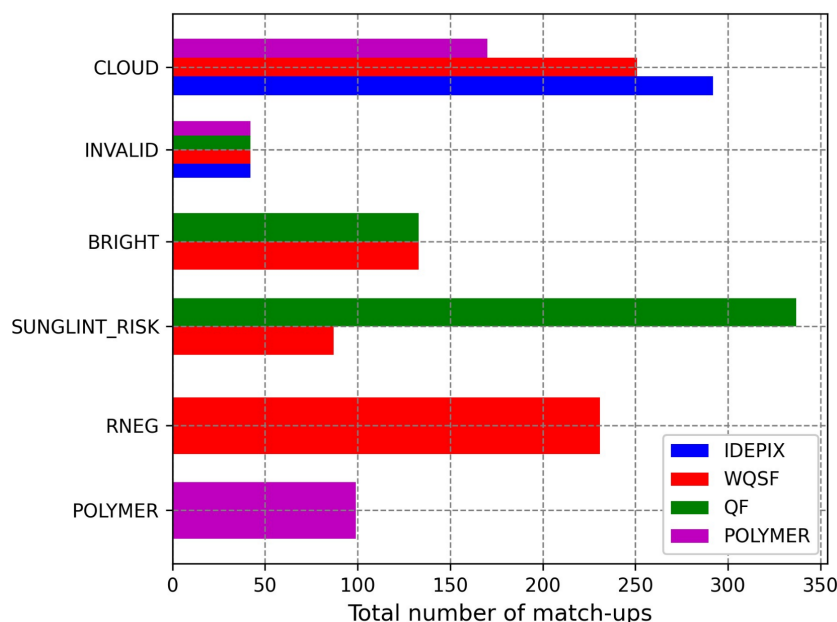


FIGURE 3

Total number of invalid match-ups with at least one pixel flagged in the 3×3 extraction window over the AERONET-OC sites. Legend colors indicate specific flag bands (IdePix: *pixeL_classif_flag*; WQSF: *wqsf*; QF: *quality_flags*; POLYMER: *bitmask*). Specific flags defining each flag output are indicated according to the subscripts of Table 2 (1: CLOUD; 2: INVALID; 3: BRIGHT; 4: SUNGLINT_RISK; 5: RNEG; 6: POLYMER).

3.2.1 AERONET-OC

Figure 4 shows the comparison between *in-situ* *Rrs* spectra from AERONET-OC sites and OLCI level-2 *Rrs* spectra processed using the four AC processors. Note that *in-situ* data for OLCI bands between 673.75 nm and 753.75 nm, as well as 885 nm, are not available using the multispectral AERONET-OC radiometers, as we limited the band shifting to a maximum of 5 nm (Table 2). Data for 1,020 nm were also excluded from the analysis because they are affected by high uncertainties in these highly absorbing waters and are not included in the OLCI level-3 dataset.

In the case of WFR, both *in-situ* and satellite median spectra keep a similar shape across the whole range, with a remarkable overlapping of the interquartile areas between 520 nm and 620 nm. In other wavelengths, WFR tends to underestimate, showing high negative deviations and higher variability in the 400–490-nm spectral range. POLYMER also shows similar spectral shapes, although it tends to overestimate across the whole spectra (except at 865 nm), with higher positive deviations between 400 nm and 490 nm. Regarding C2RCC, although satellite and *in-situ* *Rrs* spectra keep similar shapes, there is a substantial overestimation, even without any overlapping between the interquartile areas at wavelengths lower than 510 nm. Finally, despite the acceptable overlapping, the main problem of S3 FUB-CSIRO is the spectral shape, as it tends to overestimate at wavelengths lower than 510 nm but shows negative deviations in the red part of the spectrum.

The match-up scatter plots between satellite and *in-situ* AERONET-OC *Rrs* for nine OLCI bands (between 400 nm and 778.75 nm) grouped by AC processor are shown in Figure 5. The results include all the available bands for validation using AERONET-OC data except for 865 nm and 1,020 nm (Table 2).

The number of valid match-ups is lower for bands 400 nm, 510 nm, 560 nm, 620 nm, and 778.75 nm as *in-situ* data at these spectral bands were only available after 2018 (Table 2). Note also that the S3 FUB-CSIRO reflectance is not available at 400 nm and 778.75 nm.

In the blue bands (i.e., 400, 412.5, and 442.5 nm), POLYMER displays a better agreement with the *in-situ* data than other AC processors, which are affected by a marked deviation of their regression lines from the identity line (1:1). At 490 nm and 510 nm, POLYMER and S3 FUB-CSIRO perform better, whereas C2RCC and WFR tend to over- and underestimate, respectively. A good agreement is obtained at 560 nm using all the ACs except for C2RCC, which shows a positive bias. In the red part of the spectrum (i.e., 620 nm, 665 nm), the POLYMER regression line in agreement with the identity line is better than that of other ACs. Finally, at 778.75 nm, there are higher uncertainties and none of the AC processors seem to perform adequately. Nevertheless, POLYMER seems to give the best results when limiting the match-ups to low *Rrs* values ($<0.5 \cdot 10^{-3} \text{ sr}^{-1}$).

Figure 6 shows the spectral variation of some validation metrics per wavelength and AC algorithm, including also results in the infrared (i.e., 865 nm and 1,020 nm). Metric values confirm the tendencies observed in Figures 4, 5 in the visible spectral range. The WFR performance in the blue spectral region is inadequate with negative bias and RPD values and higher RMSD and lower correlation coefficients compared with other processors. However, statistical figures improve between 510 nm and 778.75 nm, being the best-performing algorithm at 560 nm. Broadly speaking, C2RCC performs worse than other AC algorithms clearly overestimating the *in-situ* *Rrs* (Figures 4, 5). It shows higher RMSD values, lower determination coefficients, and very high

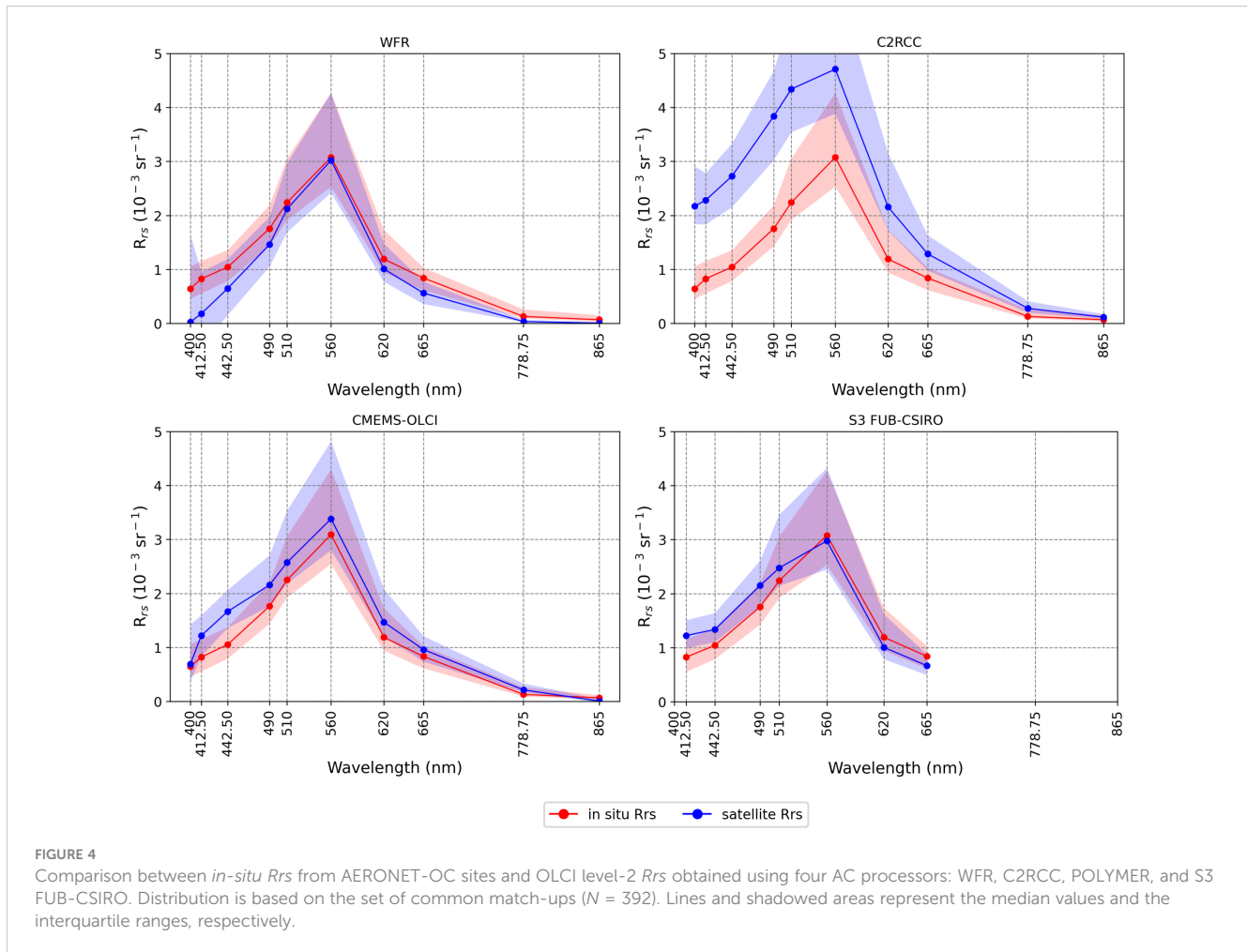


FIGURE 4

Comparison between *in-situ* R_{rs} from AERONET-OC sites and OLCI level-2 R_{rs} obtained using four AC processors: WFR, C2RCC, POLYMER, and S3 FUB-CSIRO. Distribution is based on the set of common match-ups ($N = 392$). Lines and shadowed areas represent the median values and the interquartile ranges, respectively.

positive RPD and bias values (up to 0.002 sr^{-1}), especially between 400 nm and 620 nm. On the other hand, POLYMER is the best-performing AC processor: it provides the best fitting (higher R^2) and lower error (RMSD) values (except for 442.5 nm). As observed in Figure 4, its main issue is the overestimation, showing positive RPD and bias values (lower than 0.0005 sr^{-1} except for 442.5 nm) across the visible spectral range. Finally, S3 FUB-CSIRO performs well in terms of error (RMSD) and fitting, with determination coefficients only lower than those obtained using POLYMER. Its main drawback is the spectral shape (Figure 4), with bias and RPD varying from positive to negative values with increasing wavelengths. Overall, metrics in the infrared spectral region are worse in comparison with those obtained for the visible spectral range. At 865 nm, WFR provides better results, whereas C2RCC performs better at 1,020.5 nm.

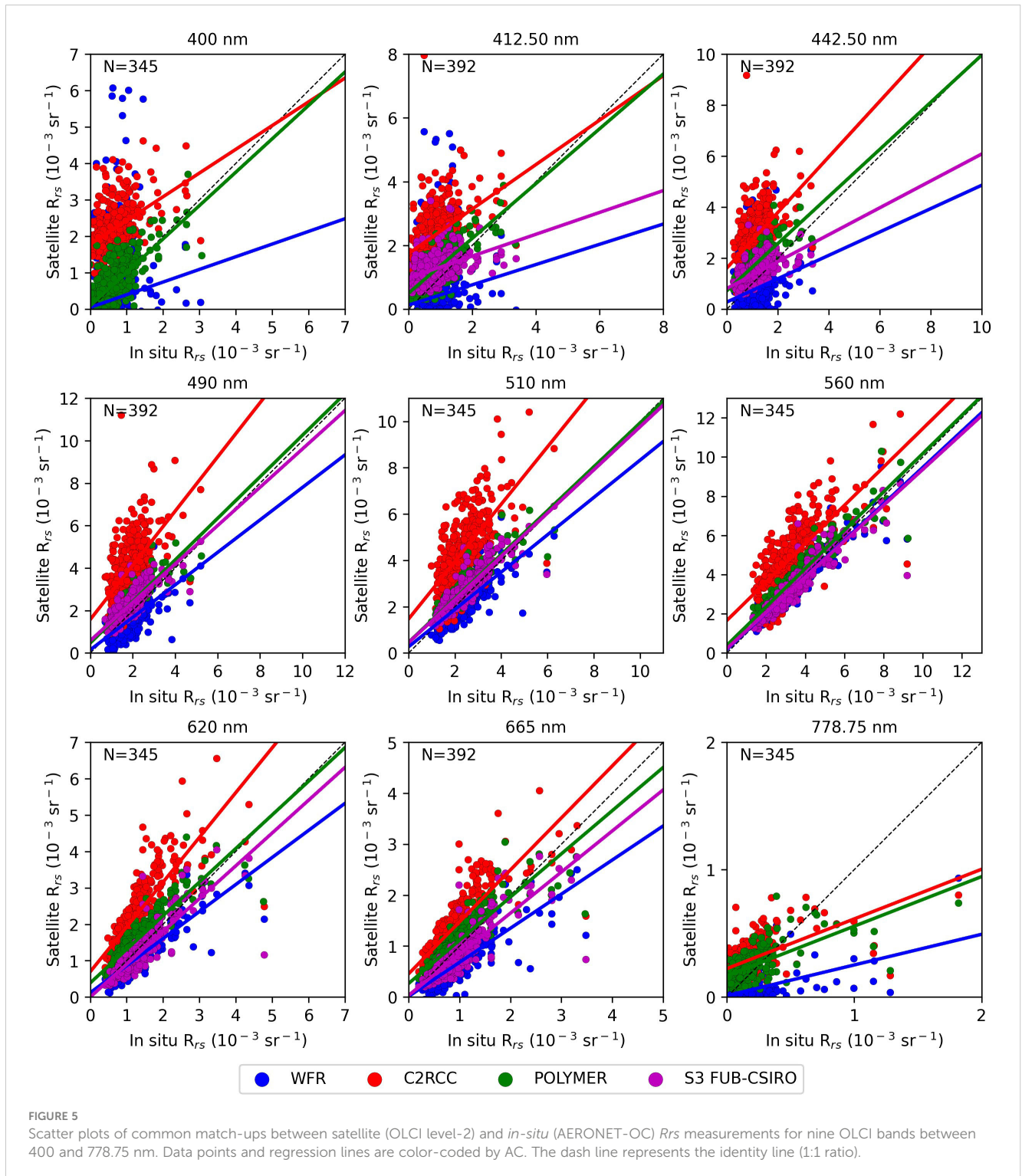
3.2.2 Shipborne radiometry

A comparison between *in-situ* R_{rs} spectra from Alg@line shipborne radiometry and OLCI level-2 R_{rs} spectra processed using the four AC processors is shown in Figure 7. In this case, as the shipborne radiometric data are hyperspectral measurements, *in-situ* data are available for all the OLCI bands. Although patterns are similar to those observed in Figure 4, some differences exist.

In detail, WFR can express well the median spectral shape, but with a higher negative bias across the bands and limited overlapping of the interquartile areas between 400 nm and 442 nm. In the case of C2RCC, it also shows extreme positive deviations for all the wavelengths, with hardly any overlapping between both distributions. S3 FUB-CSIRO follows the same pattern with a transition from positive to negative bias toward the red, but with higher uncertainties and less overlapping in the blue part of the spectrum.

Regarding POLYMER, the divergence from the reference data is more pronounced than in Figure 4: it shows negative deviations at 400 nm and 412 nm and an anomalous spectral shape between 673.75 nm and 708 nm in the three bands that are acquired at AERONET-OC sites (and hence not shown in Figure 4). For the remaining bands, they display a spectral shape agreement with a lower positive bias.

Figure 8 shows the match-up scatter plots between satellite and *in-situ* shipborne R_{rs} grouped by AC processor for the same nine OLCI bands between 400 nm and 778.75 nm shown in Figure 5. Overall, the results are worse than those obtained with the AERONET-OC sites, with the regression lines clearly deviating from the identity line (1:1). This behavior could be due to the presence of some *in-situ* spectra with very high R_{rs} values, possibly unflagged glint.



If we consider the distribution of the data points, POLYMER seems to perform better with a higher density over the identity line for all the wavelengths, although S3 FUB-CSIRO also shows good results, especially in the central wavelengths. Like AERONET-OC validation results, and as observed in Figure 7, WFR presents higher variability in the blue (wavelengths lower than 490 nm) and a better agreement in the green and red parts of the spectrum, whereas C2RCC tends to overestimate with high positive deviations across the spectra.

The spectral metrics for each processor (Figure 9) confirm the patterns observed in Figures 7, 8, as well as the validation results based on AERONET-OC *in-situ* R_{rs} . POLYMER is again the best-performing processor in the visible spectral range in terms of error (RMSD, RPD) and fitness (R^2), showing a positive bias lower than 0.0005 sr^{-1} across the spectra (except for 400 nm). As observed in Figure 7, performance is worse between 673.75 nm and 708.75 nm for the bands not validated using AERONET-OC, with lower R^2 and

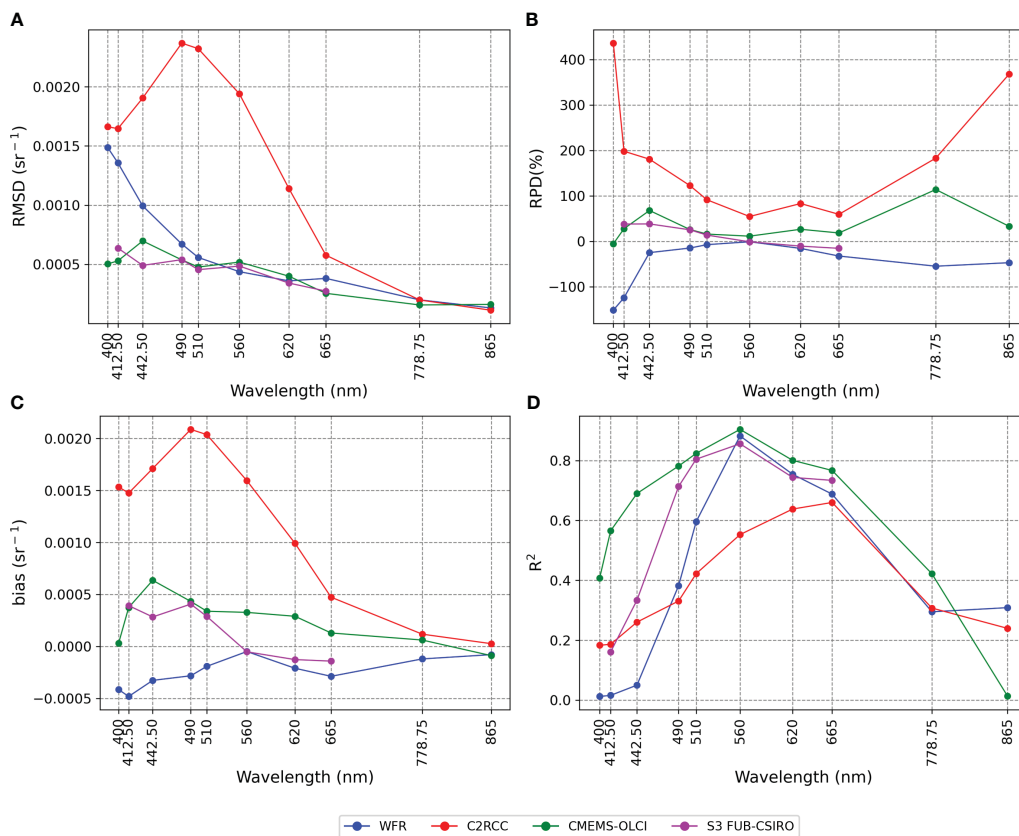


FIGURE 6

Spectral variation of the validation metrics computed for each AC from match-ups of OLCI level-2 and AERONET-OC *in-situ* *Rrs* data. (A) RMSD (in *Rrs* units: sr⁻¹). (B) Relative percent differences (%). (C) Bias (in *Rrs* units: sr⁻¹). (D) Determination coefficient (R^2 , unitless).

higher bias values. WFR does not perform well in the blue part of the spectrum, showing higher RMSD values and high negative bias compared with POLYMER or S3 FUB-CSIRO. The S3 FUB-CSIRO shows similar results to POLYMER between 560 nm and 708.75 nm, even with a better agreement (higher R^2 value) at 708.75 nm and a lower RMSD at 560 nm. However, the results are worse in terms of correlation and RMSD with wavelengths lower than 510 nm, and it cannot match the spectral shape as indicated by the decreasing bias (changing from positive to negative values) with increasing wavelengths. C2RCC, as seen in Figures 7, 8, shows a high positive bias across the whole spectra and high RMSD values with wavelengths lower than 620 nm. Overall, it performs worse than other ACs at all the wavelengths and metrics except for its higher determination coefficients between 620 nm and 708 nm. Performance metrics in the infrared (865 nm, 885 nm, and 1,020 nm) are worse than those obtained for the visible range in terms of correlation and RPD, although bias and RMSD show comparable values due to their lower *Rrs* range. WFR appears as the best-performing AC in this spectral range, with higher R^2 and lower RPD values.

3.3 Level-3 *Rrs* validation

The OLCI level-3 *Rrs* dataset was processed by merging OLCI level-2 *Rrs* obtained using POLYMER v.4.14, as it was the best-

performing AC algorithm in the Baltic Sea according to the results shown in Section 3.2. In this section, we summarize the validation results of this dataset in comparison with the multisensor level-3 *Rrs* dataset derived from OC-CCI v.6 (see Section 2.1.2) using *in-situ* radiometric measurements from AERONET-OC as reference. In addition to a common set of 433 match-ups acquired between 2016 and 2022, the results were obtained for the complete OC-CCI v.6 time series (2005–2022). Figure 10 shows the comparison between satellite and *in-situ* spectra using all the datasets and including the six bands available in OC-CCI v.6.

Using the complete time series (Figure 10A), OC-CCI v.6 captures the spectral shape across the complete spectral range with positive deviations for all the bands except for 665 nm. Similar results are observed with data from the OLCI period (Figure 10B), although the bias is close to zero or slightly negative at 560 nm with a larger overlap of the interquartile regions. CMEMS-OLCI level 3 also matches the spectral shape with positive deviations at all the bands (including 665 nm) and a relatively higher bias value at 443 nm.

Scatter plots between satellite and AERONET-OC for the same six bands comparing CMEMS-OLCI and OC-CCI v.6 (complete time series and OLCI period) are shown in Figure 11. Overall, all the datasets perform adequately in terms of fitting, especially between 490 nm and 560 nm.

As observed in Figure 10, all the datasets show positive deviations with respect to the identity line between the 412-nm

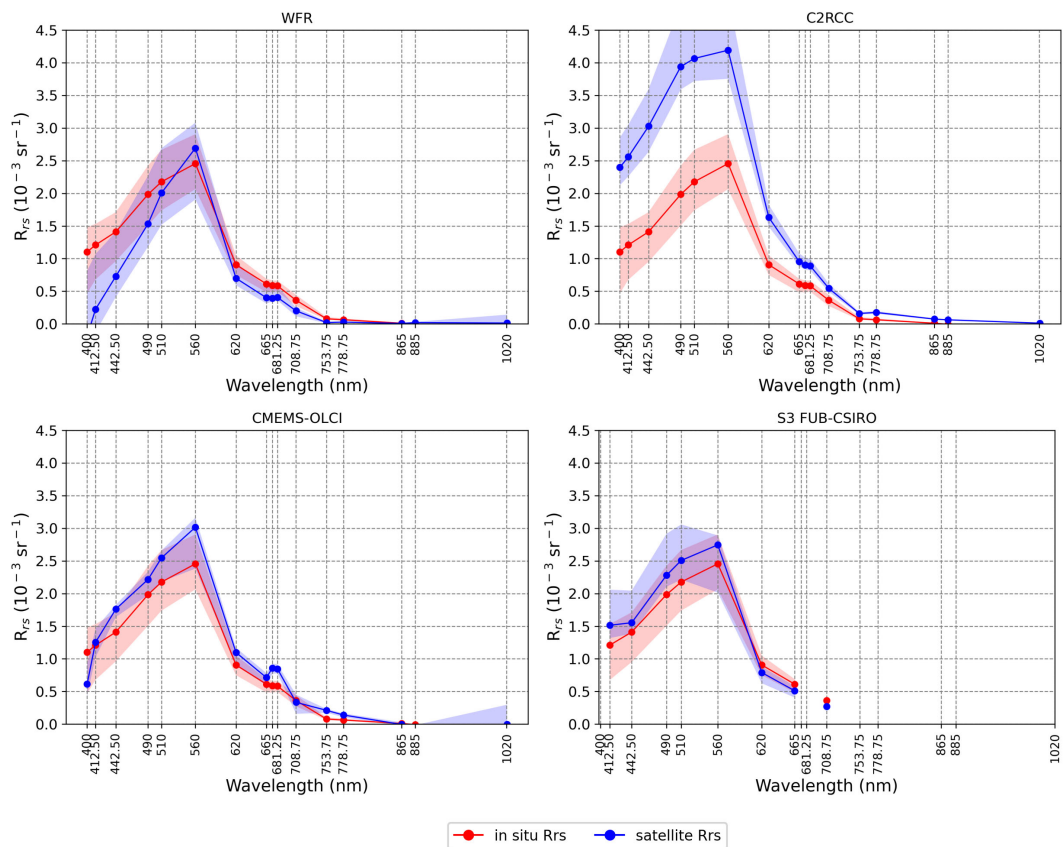


FIGURE 7

Comparison between *in-situ* R_{rs} from automated shipborne radiometry and OLCI level-2 R_{rs} obtained using four AC processors: WFR, C2RCC, POLYMER, and S3 FUB-CSIRO. Lines and shadowed areas represent the median values and the interquartile ranges, respectively.

and 490-nm spectral range, with an offset more remarkable at 443 nm. Although comparable regression fits were achieved from all the datasets, CMEMS-OLCI seems to perform better at 412 nm and 665 nm.

Figure 12 shows the spectral variation of some metrics computed from the match-ups between satellite level 3 and AERONET-OC R_{rs} .

Overall, all the metrics using the complete time series for OC-CCI v.6 are worse than those obtained only for the OLCI period, and this may be due to the differences in satellite missions being included in the OC-CCI v.6 time series and to differences related to the data availability from the three AERONET-OC sites.

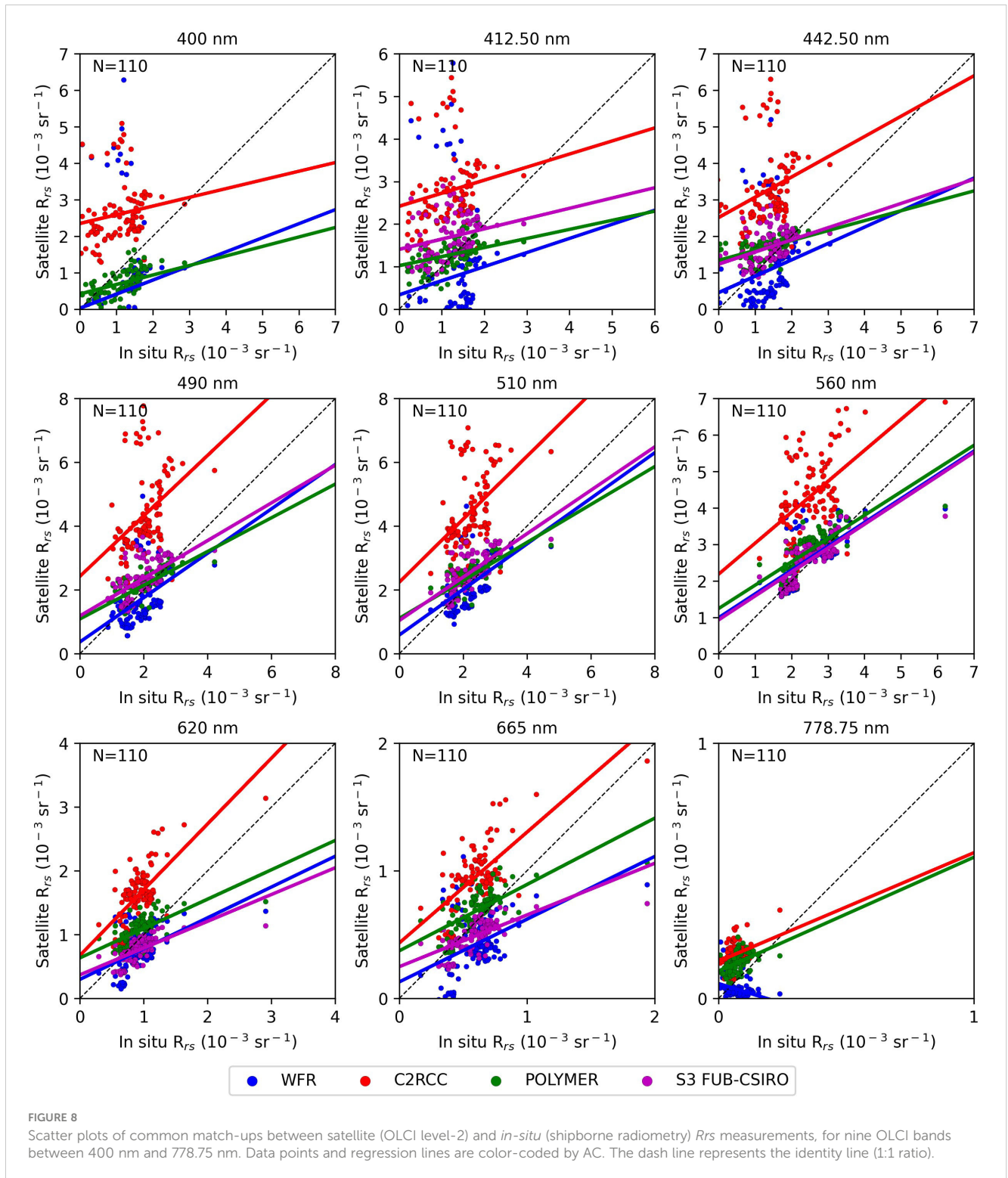
Comparing CMEMS-OLCI and OC-CCI v.6 based on the metric computed with the common set of match-ups between 2016 and 2022, CMEMS-OLCI performs better at 412 nm and OC-CCI v.6 in the 490–665-nm spectral range in terms of RMSD, RPD, and bias, whereas the results are equivalent at 443 nm. In terms of correlation, similar R^2 values were obtained for all the wavelengths except at 665 nm, with a higher R^2 (0.84 vs. 0.77) for OC-CCI v.6. In summary, both level-3 datasets perform adequately in the 490–665-nm spectral range (R^2 : 0.75–0.95; $\text{RMSD} < 0.005$) and acceptable results at 443 nm ($R^2 \sim 0.75$; $\text{RMSD} < 0.007$), whereas higher uncertainties are observed at 412 nm (Figure 12).

3.4 Chl-a validation

Chl-*a* concentrations were retrieved using the *chl-a*ENS3 ensemble approach based on R_{rs} spectra from CMEMS-OLCI and OC-CCI v.6 and validated against co-located *in-situ* chl-*a* measurements from COMBINE and Alg@line datasets. Scatter plots and main metrics are shown in Figure 13, including the results from a common set of match-ups (2016–2019) for both satellite datasets and from all the valid match-ups (1997–2019) using the complete OC-CCI v.6 time series.

Our dataset includes a total of 9,035 chl-*a* *in-situ* measurements from 1997 to 2019 (3,955 from Alg@line, 5,080 from COMBINE). For the OLCI period, only 1,047 measurements (325 from Alg@line, 722 from COMBINE) were available between 2016 and 2019. After applying the quality control (see Section 2.4), the number of valid match-ups for the OC-CCI v.6 (1997–2019) was 1,770, whereas for the OLCI period, validation for both CMEMS-OLCI and OC-CCI v.6 was based on a common set of 55 match-ups.

The results were quite comparable using the common set of match-ups, although, looking in detail, CMEMS-OLCI performs better for all performance metrics. As compared with CMEMS-OLCI, the results from the longer OC-CCI v.6 time series are characterized by a better fitness ($R^2 = 0.29$) and a lower RPD (5%), but also a higher APD (69%) and a tendency toward underestimation (bias = -0.14). These negative



deviations also appear in the results from the shorter OC-CCI v.6 time series (bias = -0.22) but are not observed in the CMEMS-OLCI dataset (bias = -0.03). Although metrics differences between both datasets could be explained by uncertainties associated with the input R_{rs} spectra, OLCI results should be interpreted with caution considering the lower number of match-ups (55 vs. 1,770) available for the OLCI period (from 2016 to 2019).

3.5 Comparison between CMEMS-OLCI and OC-CCI v.6 datasets

Figure 14 shows the scatter plots between OC-CCI v.6 and CMEMS-OLCI based on a set of co-located data points for the five R_{rs} bands involved in the chl-*a* retrieval as well as for the satellite-derived chl-*a* concentration (see Section 2.5).

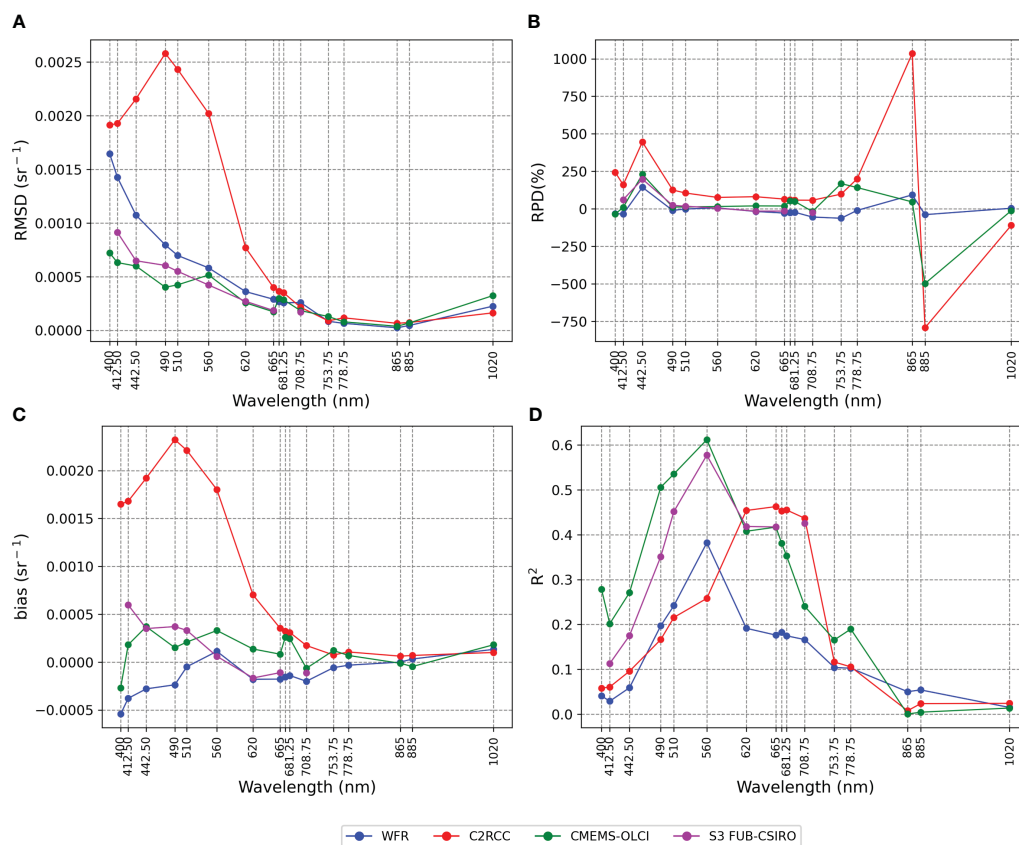


FIGURE 9

Spectral variation of the validation metrics computed for each AC from match-ups of OLCI level-2 and SYKE *in-situ* *Rrs* data. (A) RMSD (in *Rrs* units: sr⁻¹). (B) Relative percent differences (%). (C) Bias (in *Rrs* units: sr⁻¹). (D) Determination coefficient (R², unitless).

A good *Rrs* fitting with determination coefficients higher than 0.90 was observed in the 490–670-nm spectral range, whereas a poorer agreement and a higher dispersion, especially with low *Rrs* values (<5 10⁻³ sr⁻¹), were found at 443 nm. Most of the data points fall around the identity line leading to a bias value close to zero (lower than 1.9 10⁻⁴ sr⁻¹). In terms of percent error (APD and RPD), values were lower than 12% for all the bands except for 670 nm, whereas comparable RMSD values were also found for all the bands (between 2.7 10⁻⁴ and 7.6 10⁻⁴). Note that RMSD depends, to some extent, on the distribution range, so that the maximum was obtained at 443 nm (i.e., with the maximum range) and the minimum at 670 nm (minimum range) despite this band showing the maximum APD.

The scatter plots also show the data points deviating from the expected 1:1 ratio. The greatest deviation of the regression line with respect to the identity line is observed at 443 nm, caused by a significant number of points with low OC-CCI v.6 values (lower than 5 10⁻³ sr⁻¹) but high CMEMS-OLCI *Rrs* (higher than 10 10⁻³ sr⁻¹). Moreover, some erroneous data points with low CMEMS-OLCI *Rrs* (lower than 0.5 10⁻³ sr⁻¹) but OC-CCI v.6 *Rrs* values approximately 5 10⁻³ sr⁻¹ are also clearly visible in the scatter plot at 670 nm. These deviations are caused by problems with CMEMS-OLCI.

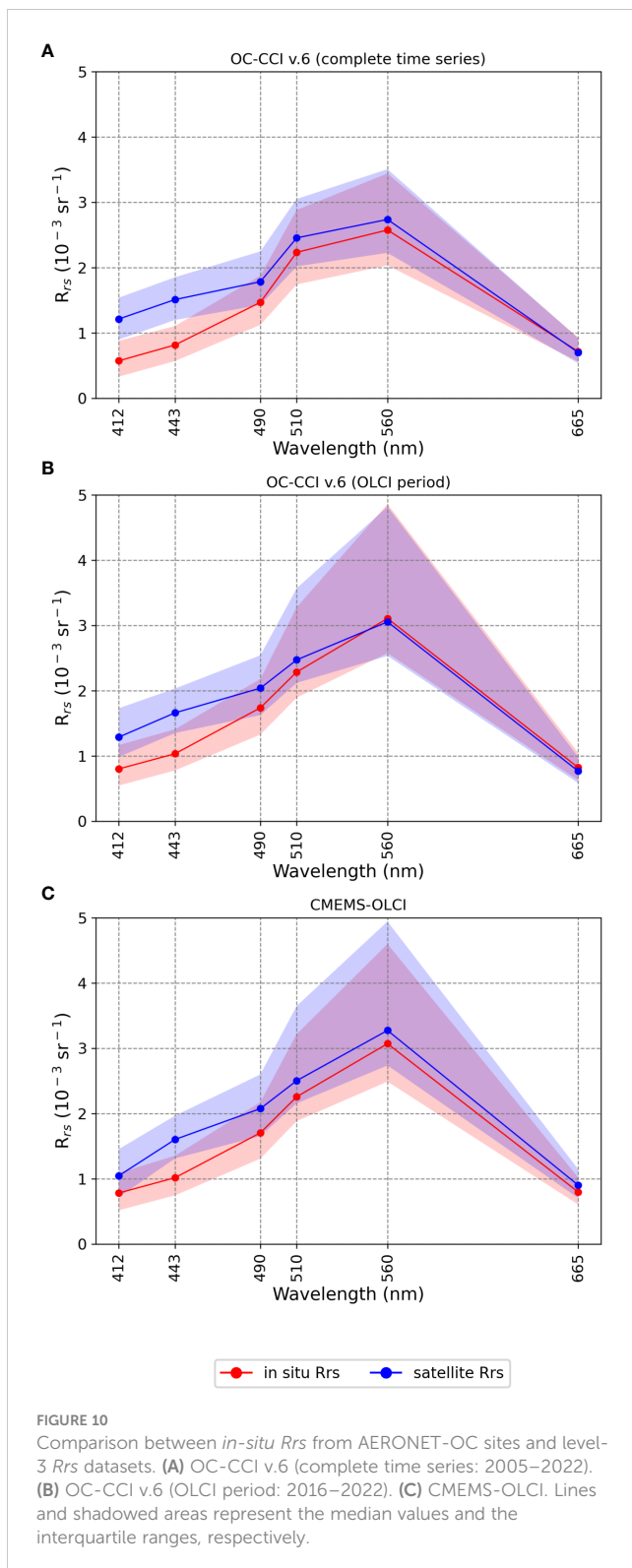
The chl-*a* concentration yielded an acceptable fitting (R² = 0.67) but with a negative bias, meaning that chl-*a* values retrieved from

OC-CCI v.6 tend to be lower than those from CMEMS-OLCI. In fact, most of the points are located below the identity line. Similar to *Rrs* at 443 nm and 670 nm, there is also a significant number of data points deviated from the expected 1:1 ratio, with concentrations ranging from 1.5 mg m⁻³ to 15 mg m⁻³ from OC-CCI v.6 but values lower than 0.5 mg m⁻³ when retrieved from CMEMS-OLCI.

4 Discussion

This study presented the introduction within the Copernicus Marine Service of the operational *Rrs* and chl-*a* datasets for the Baltic Sea from OLCI full resolution (300 m). Poor performances have been reported in the assessment of OLCI *Rrs* for the Baltic CDOM-dominated waters using both the EUMETSAT Operational Baseline (Zibordi et al., 2018; Zibordi et al., 2022) and the alternative atmospheric correction processing chain based on CR2CC (Cazzaniga et al., 2022). Hence, the first step was to select the best AC method to retrieve OLCI *Rrs* by comparing the accuracy of four processors using *in-situ* radiometric data from AERONET-OC sites and Alg@line shipborne hyperspectral radiometry as reference.

Our validation results from both *in-situ* sources (fixed platform and shipborne observations) show that POLYMER v.4.14 was the best option for the implementation in the processing chain for the



new level-3 OLCI R_{rs} and *chl-a* datasets (see Section 3.2). In fact, it performs better not only in the 443–665-nm spectral range which includes the relevant bands for *chl-a* retrieval (Table 1), but also at 400 nm, 412.5 nm, and 778.75 nm. A greater variability in the metrics in the 673.75–708.75-nm spectral range (validated only with shipborne radiometry) and at 865 nm hinders the

identification of the best-performing AC in this spectral range. Overall, performance differences are more remarkable in the blue spectral region (400–490 nm), especially in terms of correlation (Figures 6, 9). The main drawback for *chl-a* retrieval is the positive bias observed from both sources across the 412.5–665-nm spectral range.

Although validation results from AERONET-OC sites are expected to be more robust and reliable as *in-situ* data come from a stable platform with fewer uncertainties, metrics based on shipborne radiometry collected in 2016 were consistent and show the potential of this method to increase the number of match-ups providing data at other sites with different atmospheric and/or water conditions. According to Tilstone et al. (2022), differences between both *in-situ* sources could be mainly explained by two factors: 1) site differences—Baltic Sea waters are mainly dominated by CDOM, but ship trajectories could be more influenced by increases in *chl-a* concentrations due to phytoplankton blooms, whereas CDOM concentrations are generally higher in AERONET-OC sites; and 2) instruments and data processing—the differences in instruments (TriOS-RAMSES in the case of the hyperspectral shipborne radiometry; CIMEL-SeaPRISM for AERONET-OC) with their specific uncertainties by wavelength may be augmented by the fact that the data are processed with distinct methodologies. Moreover, in our study, shipborne radiometry is only available for validating Sentinel-3A in 2016, as AERONET-OC *in-situ* data extend from 2016 to 2022 enabling the validation of both Sentinel-3A and Sentinel-3B.

In our study, POLYMER results from AERONET-OC as compared with Alg@line in the 442.5–665-nm spectral range were better in terms of correlation (0.41–0.90 vs. 0.19–0.61), but slightly worse considering RMSD ($2.6\text{--}7.0 \cdot 10^{-4} \text{ sr}^{-1}$ vs. $1.7\text{--}6.0 \cdot 10^{-4} \text{ sr}^{-1}$) or bias ($1.3\text{--}6.4 \cdot 10^{-4} \text{ sr}^{-1}$ vs. $0.8\text{--}3.7 \cdot 10^{-4} \text{ sr}^{-1}$). As RPD are similar from the two sources (between 10% and 28% except for 442.5 nm), higher RMSD or bias values using AERONET-OC could also be related to its larger *in-situ* R_{rs} range and maximum values (see *in-situ* distribution in Figures 4, 7). Moreover, overall better results according to all the metrics were derived from AERONET-OC at 400 nm, 412.5 nm, and 778.75 nm (except for RMSD at 412.5 nm). At 400 nm, a negative bias was obtained from Alg@line ($-2.7 \cdot 10^{-4} \text{ sr}^{-1}$) but a positive value ($3.2 \cdot 10^{-5} \text{ sr}^{-1}$) from AERONET-OC, which could be related to differences in optical water characteristics: higher CDOM concentrations leading to lower R_{rs} (and higher bias) in AERONET-OC sites. In fact, only 21% of match-ups from AERONET-OC show R_{rs} greater than $1 \cdot 10^{-3} \text{ sr}^{-1}$ against 55% from the shipborne radiometry.

Another remarkable feature is the high RPD peak at 442 nm from shipborne radiometry, which is present in all the processors. This peak is explained by a small set of match-ups with very high RPD values (>200% with a maximum of approximately 23,000%) from 2 days (9 June 2016 and 28 July 2016). These high RPD values are caused by some outliers in the *in-situ* distribution at 442 nm characterized by very low R_{rs} values ($0.06\text{--}0.86 \cdot 10^{-3}$), as compared with the interquartile range between $1.25 \cdot 10^{-3}$ and $1.75 \cdot 10^{-3} \text{ sr}^{-1}$ (Figure 7). These results evidence that results from shipborne radiometry could be improved by a stricter *in-situ* quality control

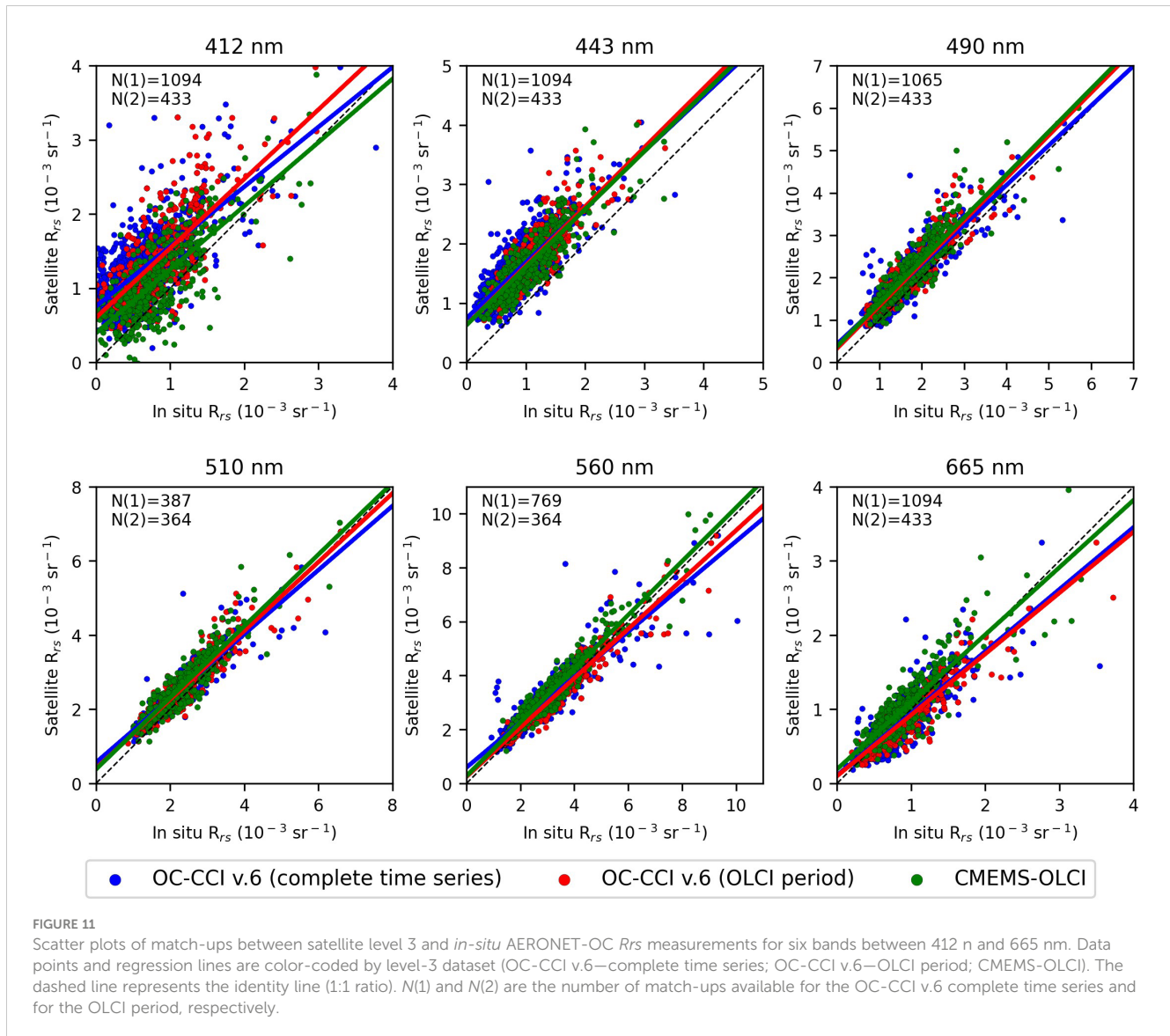


FIGURE 11

Scatter plots of match-ups between satellite level 3 and *in-situ* AERONET-OC R_{rs} measurements for six bands between 412 nm and 665 nm. Data points and regression lines are color-coded by level-3 dataset (OC-CCI v.6—complete time series; OC-CCI v.6—OLCI period; CMEMS-OLCI). The dashed line represents the identity line (1:1 ratio). $N(1)$ and $N(2)$ are the number of match-ups available for the OC-CCI v.6 complete time series and for the OLCI period, respectively.

(e.g., removing spectra with outliers). However, this refinement is out of the scope of this work as we use the dataset as a method to confirm the conclusions based on AERONET-OC data.

POLYMER also shows advantages in terms of coverage in comparison with other AC methods as by design it is able to deal with residual sun glint (Steinmetz and Ramon, 2018). As seen in Table 3, the number of valid match-ups based only on POLYMER flag mask *bitmask* (846 valid match-ups from AERONET-OC) or combining *bitmask* and *IdePix* (773 valid match-ups from AERONET-OC) is 30% higher than those using other processors. However, yielding more match-ups does not imply a better or worse performance of the validation results. In fact, datasets showed similar distributions, with close ranges and median values across the spectra. Table 4, based on AERONET-OC *in-situ* data, presents comparable values for R^2 , RMSD, or bias in the 412.5–665-nm spectral range, whereas expected higher uncertainties were observed at 400 nm or 778.75 nm. Note that bias was consistently lower across the whole spectra using only *bitmask*, especially in the blue, meaning that extra match-ups produced by POLYMER tend to show a lower bias.

Table 4 also shows the differences between the POLYMER validation metrics from Sentinel-3A and Sentinel-3B using *in-situ* data from AERONET-OC. Overall, results from Sentinel-3A are better considering all the metrics across the spectra, except for the bias between 620 nm and 778.75 nm. Differences are expected since match-up datasets do not show the same spatial–temporal coverage leading to different numbers of valid match-ups as Sentinel-3B is only available from 2018.

Our level-2 validation results agree with the findings in other works comparing AC algorithms over the Baltic Sea. Tilstone et al. (2022) assessed Sentinel-3A R_{rs} from WFR (pb 2.23–2.29 and OL_L2M.003), POLYMER v.4.14, and C2RCC using *in-situ* data from Alg@line shipborne radiometry (199 match-ups), Gustav Dalen Tower (5 match-ups), and Helsinki Lighthouse (4 match-ups), all the match-ups for only 2016. They found that POLYMER was the best-performing AC algorithm for six bands (412 nm, 443 nm, 490 nm, 560 nm, 665 nm, and 709 nm). Alikas et al. (2020) validated satellite OLCI R_{rs} from four AC processors (i.e., ALTNN, C2RCC, POLYMER, and WFR) against above-water field

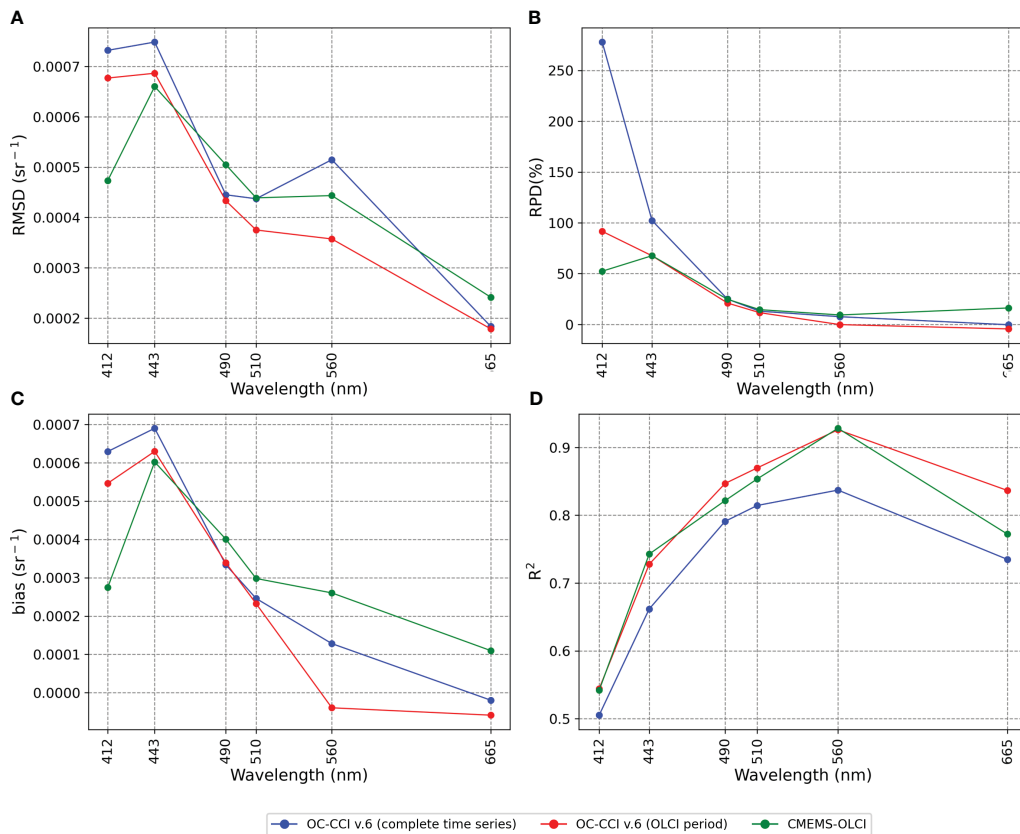


FIGURE 12 Spectral variation of the validation metrics computed from match-ups of level-3 datasets (OC-CCI v.6 complete time series; OC-CCI v.6–OLCI period; CMEMS-OLCI) and AERONET *in-situ* R_{rs} data. **(A)** RMSD (in R_{rs} units: sr^{-1}). **(B)** Relative percent differences (%). **(C)** Bias (in R_{rs} units: sr^{-1}). **(D)** Determination coefficient (R^2 , unitless).

measurements collected from a research vessel over the coast of the Baltic Sea and Estonian Lakes in 2016. With a number of valid match-ups between 15 and 49 depending on the AC processor and filtering level, they reported POLYMER as the best suitable algorithm for all the OLCI bands except for 865 nm.

Since most of the valid match-ups (199 of 208) in [Tilstone et al. \(2022\)](#) are derived from the same dataset based on shipborne

radiometry, metric values are expected to be similar to those reported in Section 3.2.2. In fact, RMSD values ($2\text{--}6 \cdot 10^{-4} \text{ sr}^{-1}$ in this work; $3\text{--}7 \cdot 10^{-4} \text{ sr}^{-1}$ in [Tilstone et al., 2022](#)) or Pearson correlation coefficients (0.45–0.78 in this work; 0.38–0.6) follow a similar pattern. Differences are mainly observed in the bias, with negative values in [Tilstone et al. \(2022\)](#) ($-4 \cdot 10^{-4}$ to $-1 \cdot 10^{-4} \text{ sr}^{-1}$) instead of the positive bias found in our work ($8 \cdot 10^{-5}$ to $4 \cdot 10^{-4}$).

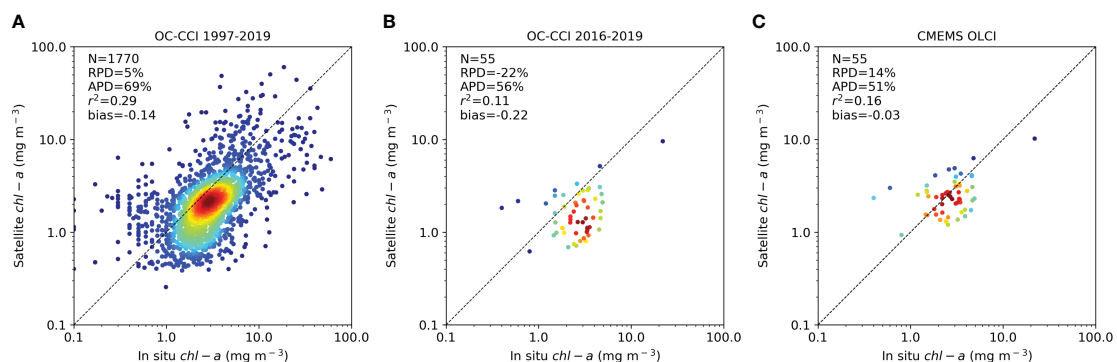
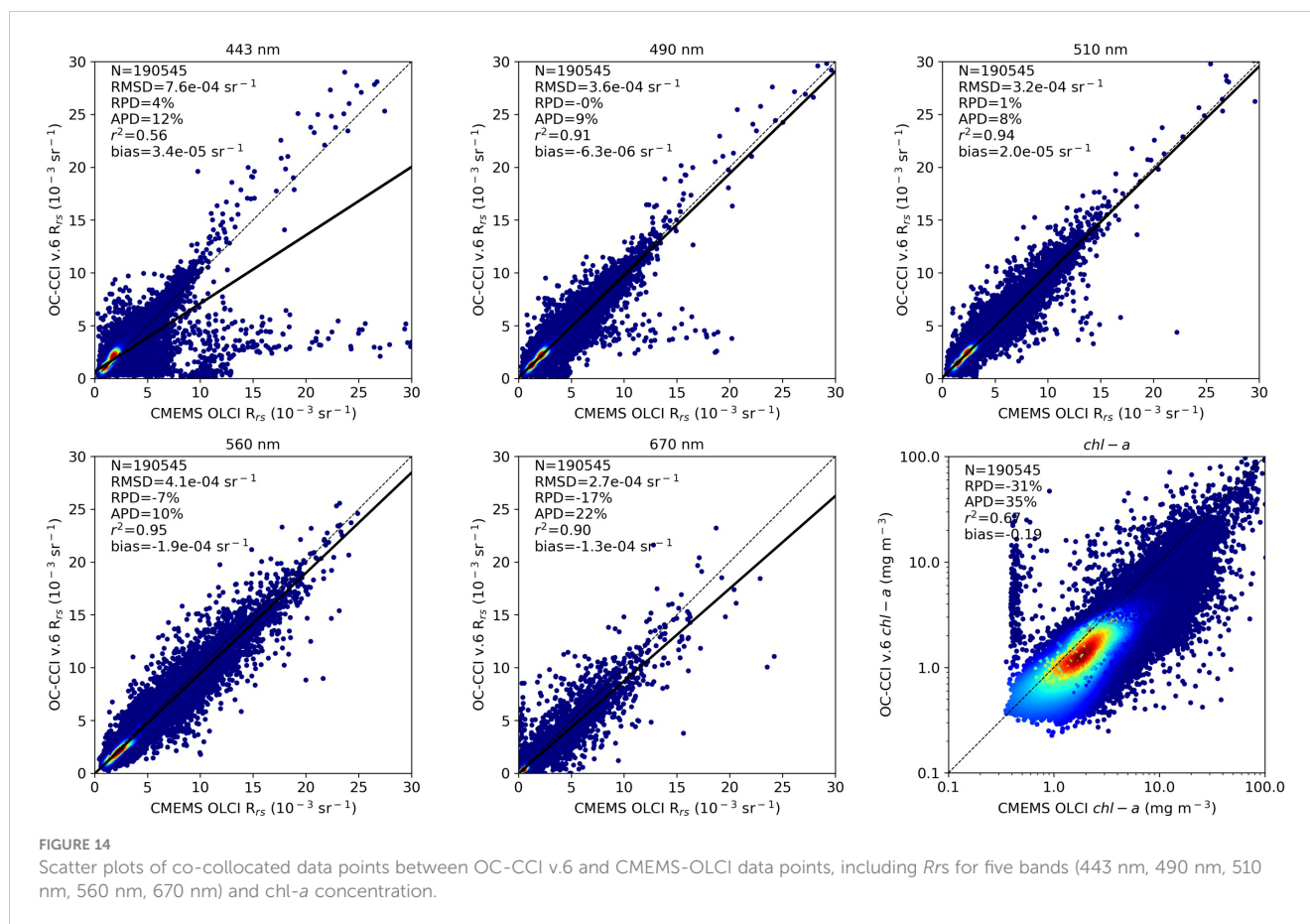


FIGURE 13 Scatter plots of match-ups between satellite-derived and *in-situ* log-transformed $chl-a$ measurements. Satellite $chl-a$ concentrations were retrieved using *chl-a*ENS3. **(A)** all the valid match-ups (1997–2019) from OC-CCI v.6; **(B)** common match-ups (2016–2019) for OC-CCI v.6; and **(C)** CMEMS-OLCI. Data points are colored by density. The continuous line represents the 1:1 ratio.



This disparity could be explained because we applied a stricter validation protocol with results based on a dataset of common match-ups, leading to a considerably lower number of match-ups (107 vs. 199 in Tilstone et al.). Relaxing our protocol using only *bitmask* as flag band, the number of valid match-ups increases until 251 and bias tends to be lower (likewise using the AERONET-OC dataset), so that comparable negative bias values ($-8.9 \cdot 10^{-5}$ to $-1.4 \cdot 10^{-4}$) were found in the 490–665-nm spectral range.

Regarding the level-3 datasets, the *in-situ* distribution for the complete OC-CCI v.6 time series (Figure 10A) is characterized by lower R_{rs} values at 490 and 560 nm in comparison with the OLCI period (Figures 10B, C). Differences are more remarkable at 560 nm, with an upper quartile value approximately $3.5 \cdot 10^{-3} \text{ sr}^{-1}$ against a peak of almost $5 \cdot 10^{-3} \text{ sr}^{-1}$. These discrepancies could be explained by two facts. Firstly, differences in the optical water types related to the data availability from the three AERONET-OC sites: the complete time series include more spectra from Helsinki Lighthouse, whereas *in-situ* data from Irbe Lighthouse (available since 2018) become more predominant during the OLCI period as measurements at the Helsinki Lighthouse ended in 2019. Secondly, the results at 560 nm for the complete time series use *in-situ* data from the AERONET-OC band at 555 nm available between 2005 and 2011, introducing uncertainties associated with the band-shifting process. However, the results for the OLCI period are only based on the AERONET-OC band at 560 nm introduced in 2018 (Table 1).

Using the common set of match-ups, CMEMS-OLCI and multisensor OC-CCI v.6 show equivalent distributions and metrics (with some differences indicated in Section 3.3) notwithstanding the different spatial resolution (300 m vs. 1 km). This similar behavior could be explained because both datasets are based on the same AC processor, i.e., POLYMER (with the exception of SeaWiFS), and that from 2020 onward, OC-CCI v.6 is based only on OLCI from Sentinel-3A and Sentinel-3B, as MODIS-AQUA and VIIRS are included only until the end of 2019 (OC-CCI, 2022). As expected, the metrics from CMEMS-OLCI L3 (Figure 6) are very close to those from POLYMER OLCI L2 (Figure 12).

Our results based on the complete OC-CCI v.6 time series differ from the metrics for OC-CCI v.4.2 reported in Brando et al. (2021). OC-CCI v.6 performs better in terms of correlation for the 412–490-nm spectral range, whereas R^2 values are similar for the other bands, with more remarkable differences at 400 nm (0.51 vs. 0.05) and 442.5 nm (0.66 vs. 0.34). However, OC-CCI v.4.2 shows lower positive bias values ($0.1 \cdot 10^{-4}$ – $0.8 \cdot 10^{-4} \text{ sr}^{-1}$ against $1.2 \cdot 10^{-4}$ – $6.9 \cdot 10^{-4} \text{ sr}^{-1}$) and performs better in terms of APD or RPD in the 412–560-nm spectral range. Finally, OC-CCI v.6 shows lower bias, APD, and RPD at 665 nm.

The main differences between both OC-CCI versions explaining these discrepancies are the change of reference sensor from SeaWiFS to MERIS, the introduction of OLCI from Sentinel-3A and Sentinel-3B, and the shift of the green band from 555 nm to 560

TABLE 4 Validation metrics for eight OLCI wavelengths in the visible spectral range.

	400*	412.5	442.5	490	510*	560*	620*	665	778.75
POLYMER L2 common match-ups (N = 392; N* = 354)									
R ²	0.41	0.57	0.69	0.78	0.82	0.9	0.8	0.77	0.74
RMSD	5.0	5.3	7.0	5.4	4.8	5.2	4.0	2.6	3.5
Bias	0.3	3.8	6.4	4.3	3.4	3.3	2.9	1.3	0.6
POLYMER L2 bitmask (N = 846; N* = 754)									
R ²	0.36	0.53	0.69	0.77	0.81	0.88	0.76	0.7	0.35
RMSD	5.1	5.1	6.9	5.3	4.7	5.2	4.0	2.7	1.6
Bias	0.0	3.3	6.3	4.1	3.1	2.7	2.6	1.0	0.5
POLYMER L2 common match-ups—SENTINEL-3A (N = 428; N* = 342)									
R ²	0.43	0.57	0.74	0.82	0.87	0.93	0.86	0.8	0.46
RMSD	4.6	4.5	6.7	5.1	4.4	4.5	3.7	2.3	1.2
Bias	-0.1	2.8	6.2	4.2	3.3	2.8	2.9	1.2	0.6
POLYMER L2 common match-ups—SENTINEL-3B (N = 345; N* = 345)									
R ²	0.39	0.54	0.66	0.74	0.80	0.86	0.73	0.68	0.36
RMSD	5.1	5.7	7.2	5.6	4.9	5.7	4.3	2.9	1.7
Bias	0.7	4.2	6.5	4.3	3.3	3.0	2.7	1.1	0.5
CMEMS L3—Gustav Dalen Tower (N = 241; N* = 206)									
R ²		0.57	0.74	0.81	0.86	0.91		0.73	
RMSD		4.7	6.9	5.2	4.7	5.2		2.5	
Bias		2.9	6.4	4.3	3.4	3.0		1.1	
CMEMS L3—Helsinki Lighthouse (N = 90; N* = 39)									
R ²		0.51	0.68	0.77	0.84	0.91		0.78	
RMSD		4.2	6.4	5.2	5.7	6.2		2.6	
Bias		2.4	5.8	4.2	4.5	4.2		1.1	
CMEMS L3—Irbe Lighthouse (N = 155; N* = 155)									
R ²		0.36	0.63	0.74	0.80	0.92		0.72	
RMSD		5.2	6.5	4.8	3.9	3.9		2.5	
Bias		2.8	5.7	3.4	1.9	1.4		0.9	

Match-ups based on AERONET-OC in-situ Rrs. *Wavelengths with in-situ data only from 2018. R²: unitless. RMSD and bias: in 10⁻⁴ sr⁻¹.

nm. Moreover, the results in Brando et al. (2021) include 680 match-ups from 2005 to 2019, most of them from Gustav Dalen Tower and Helsinki Lighthouse, as the results from v.6 until 2022 introduce more *in-situ* data from Irbe Lighthouse. Note also that a stricter quality control (9 valid pixels in the extractions window instead of 4) was introduced in this work.

Table 4 shows the metrics from CMEMS-OLCI Rrs for the three sites. Overall, all of them are characterized by CDOM-dominated waters, and the metrics follow the same spectral pattern. The results from Gustav Dalen Tower and Helsinki Lighthouse lead to similar results, with more match-ups and a better adjustment (R²) from Gustav Dalen Tower. In the case of Irbe Lighthouse, the results show a poorer agreement at 412.5 nm and lower RMSD and bias in

the 490–560-nm spectral range, which could be explained by a lower Rrs range.

OC-CCI v.6 chl-*a* retrievals show validation results (R² = 0.29; RPD = 5%; APD = 69%; bias = -0.14), consistent with those reported for the previous version of the multisensor level-3 processing chain, i.e., OC-CCI v.4.2 (Brando et al., 2021: R² = 0.24; RPD = 41%; APD = 90%; bias = -0.78), with a better performance considering all the metrics. Overall, the effect of the positive bias observed in the 412–510-nm spectral range (Figures 12, 13) seems to be adequately handled by the ensemble approach.

Chl-*a* validation results from CMEMS-OLCI are similar to those from OC-CCI v.6 using the common set of match-ups (Figure 13). The most remarkable difference is the lower bias

(−0.03 against −0.22), which is consistent with the bias decrease with the introduction of OLCI in the multisensor level-3 datasets from −0.78 (OC-CCI v.4.2, without OLCI, [Brando et al., 2021](#)) to −0.22 (OC-CCI v.6, with OLCI, this work). In any case, further research is required because of the small number of chl-*a* match-ups available for the OLCI period.

Scatter plots of co-located OC-CCI v.6 and CMEMS-OLCI data points ([Figure 14](#)) show better statistical figures for *Rrs* (except for 443 nm) than chl-*a*. Note that OC-CCI v.6 *Rrs* are derived from different space sensors and AC, whereas CMEMS-OLCI *Rrs* are obtained from Sentinel-A and Sentinel-B images processed with POLYMER v.4.14. With the exclusion of outliers, which are possibly related to the resolution and coverage of both datasets, most *Rrs* differences can be attributed to the specificities of data processing and absolute radiometric accuracy of the reference sensor (MERIS for OC-CCI v.6 and OLCI for CMEMS-OLCI).

An overall good agreement was found in the comparison between chl-*a* retrievals from CMEMS-OLCI and OC-CCI v.6, with a tendency of CMEMS-OLCI toward greater chl-*a* concentrations ([Figure 14](#)).

Nevertheless, the differences in *Rrs* are amplified in terms of chl-*a* retrieval. This is probably due to the non-linear nature of the MLP retrievals of chl-*a* and of the weights in the *chl-aENS3* ensemble approach adopted in this study, as well as the underlying relationship between apparent and inherent optical properties in the Baltic Sea.

An issue is the presence of erroneous data points caused by underestimation in the chl-*a* retrievals from CMEMS-OLCI (<0.5 mg m^{−3}) as compared with OC-CCI v.6 (1.5–15 mg m^{−3}) ([Figure 14](#)). These wrong retrievals are caused by anomalously high OLCI *Rrs* values with a smaller range at 490 nm (4–5 10^{−3} sr^{−1} in CMEMS-OLCI against 0.01–3.5 10^{−3} sr^{−1} in OC-CCI v.6) and 510 nm (3–3.25 10^{−3} sr^{−1} in CMEMS-OLCI against 0.01–2.5 10^{−3} sr^{−1} in OC-CCI v.6). Note that these points are not clearly visible in the scatter plots in [Figure 14](#).

Potential differences in the validation results between the available datasets (i.e., COMBINE and Alg@line, see Section 2.2.2), as well as differences in the analytical methods and protocols for the chl-*a* concentration estimation, were not considered in this study because of the limited number of match-ups, mainly for the OLCI period. It should be noted that [Brando et al. \(2021\)](#) reported higher uncertainty for the match-ups of their multisensor time series with the COMBINE measurements as compared with Alg@line water samples due to different sampling strategies and dynamic ranges of both data sources.

In our sampling to perform the comparative analysis (a point every 10 km, an image every 10 days, see Section 2.5), only 143 points (of 190,546) from 32 images (of 240) were identified as erroneous. For most of the images, only one erroneous point was found, with a maximum of 28 points on a single image. Despite this low impact, further research with a full sampling is required to evaluate the actual effect of these wrong pixels and to implement a flagging procedure.

Regarding wrong *Rrs* values with a lower impact on the chl-*a* results (e.g., at 442 nm or 670 nm, see [Figure 14](#)), the presence in our sampling is limited to a small number of points by image (often only one). For instance, we identified 216 erroneous points in 64 images at 442 nm and only 32 points in 18 images at 660 nm. In any case, likewise chl-*a*, a further masking could improve the mapping results.

5 Conclusions

In this study, the performance of four atmospheric correction processors for the *Rrs* retrieval from Sentinel-3 OLCI was assessed within the development of the regional ocean color processing chain for the Baltic Sea. The validations with the *in-situ* measurements collected at three AERONET-OC sites and those relying on the Alg@line shipborne hyperspectral radiometry show that POLYMER v.4.14 was the best-performing processor in terms of error and fitness in the visible spectral range, as well as spatial coverage. Results also document the relevance of shipborne radiometry to complement *in-situ* measurements from fixed sites, allowing for a larger spatial footprint across all subbasins.

POLYMER-derived *Rrs* spectra were thus employed to retrieve chl-*a* from OLCI full-resolution (300 m) data using the bio-optical ensemble scheme already introduced in the CMEMS processing chain for the Baltic Sea. Additionally, this study evaluated the operational *Rrs* and chl-*a* multiyear time series (from 1997 to 2022) for the Baltic Sea based on OC-CCI v.6.

The chl-*a* values retrieved from OC-CCI v.6 and OLCI *Rrs* using the same regional bio-optical ensemble scheme were compared with the *in-situ* chl-*a* measurements. Results confirm previous analyses undertaken within the CMEMS products assessments, even if the number of OLCI match-ups (2016–2019) was lower. A study extension is planned to include more recent *in-situ* measurements once available.

Finally, an overall good agreement was found in the comparison between chl-*a* retrievals from OLCI and OC-CCI v.6. However, differences between the *Rrs* bands used as input for the bio-optical ensemble scheme were amplified in terms of chl-*a* retrieval. A flagging strategy should be devised to identify and reduce the presence of erroneous data points in both datasets. Furthermore, a sensitivity analysis is then part of the future developments to analyze the response of the bio-optical ensemble by adding synthetic offsets and noise to input *Rrs* spectra and verify how it affects the chl-*a* retrieval.

Our results confirm that the quality of operational ocean color datasets presented in this study is suitable for studies on phytoplankton phenology, bloom occurrence, water quality monitoring, and eutrophication assessment in this threatened ecosystem.

Data availability statement

The datasets presented in this study can be found in online repositories. The names of the repository/repositories and accession number(s) can be found below: E.U. Copernicus Marine Service Information (CMEMS) Marine Data Store (MDS: marine.copernicus.eu): OCEANCOLOUR_BAL_BGC_L3_NRT_009_131 (Baltic Sea Ocean Colour Plankton, Reflectances, Transparency and Optics L3 NRT daily observations). E.U. Copernicus Marine Service Information (CMEMS). Marine Data Store (MDS). DOI: 10.48670/moi-00294 (Accessed on 10-JUL-2023) OCEANCOLOUR_BAL_BGC_L3_MY_009_133 (Baltic Sea Multiyear Ocean Colour Plankton, Reflectances and Transparency L3 daily observations). E.U. Copernicus Marine Service Information (CMEMS). Marine Data Store (MDS). DOI: 10.48670/moi-00296 (Accessed on 10-JUL-2023).

Author contributions

LG: Conceptualization, Data curation, Formal analysis, Software, Validation, Visualization, Writing – original draft. VB: Conceptualization, Formal analysis, Funding acquisition, Methodology, Project administration, Software, Supervision, Validation, Visualization, Writing – original draft. ADC: Data curation, Writing – review & editing. SC: Data curation, Software, Writing – review & editing. DD'A: Conceptualization, Funding acquisition, Methodology, Software, Supervision, Writing – review & editing. TK: Writing – review & editing. JA: Data curation, Writing – review & editing. TS: Writing – review & editing.

Funding

The author(s) declare financial support was received for the research, authorship, and/or publication of this article. This work has been performed in the context of the Ocean Colour Thematic Assembly Centre of the Copernicus Marine Environment and Monitoring Service (contract: 21001L02-COP-TAC OC-2200– Lot 2: Provision of Ocean Colour Observation Products (OC-TAC)) and the HYPERNETS project funded by the European Union's Horizon 2020 research and innovation programme (Grant agreement no 775983).

Acknowledgments

EUMETSAT is acknowledged for the provision of the Copernicus Sentinel-3 full-resolution data. The Plymouth Marine Laboratory made available the OC-CCI v.6 *Rrs* spectra at 1 km

References

- Ahlman, M., Alenius, P., Attila, J., Arnkil, A., Arponen, H., Below, A., et al. (2020). *Seurantakäsikirja suomen merenhoitosuunnitelman seurantaohjelmaan vuosille 2020–2026 (Manual for marine monitoring in Finland 2020–2026)* (Helsinki, Finland: Suomen Ympäristökeskus).
- Alikas, K., Ansko, I., Vabson, V., Ansper, A., Kangro, K., Uudeberg, K., et al. (2020). Consistency of radiometric satellite data over lakes and coastal waters with local field measurements. *Remote Sens.* 12 (4), 616. doi: 10.3390/rs12040616
- Andersen, J. H., Axe, P., Backer, H., Carstensen, J., Claussen, U., Fleming-Lehtinen, V., et al. (2011). Getting the measure of eutrophication in the baltic sea: towards improved assessment principles and methods. *Biogeochemistry* 106, 137–156. doi: 10.1007/s10533-010-9508-4
- Attila, J., Koponen, S., Kallio, K., Lindfors, A., Kaitala, S., and Ylöstalo, P. (2013). MERIS Case II water processor comparison on coastal sites of the northern Baltic Sea. *Remote Sens. Environ.* 128, 138–149. doi: 10.1016/j.rse.2012.07.009
- Beltrán-Abaunza, J. M., Kratzer, S., and Brockmann, C. (2014). Evaluation of MERIS products from Baltic Sea coastal waters rich in CDOM. *Ocean Sci.* 10, 377–396. doi: 10.5194/os-10-377-2014
- Berthon, J.-F., and Zibordi, G. (2010). Optically black waters in the Northern Baltic Sea. *Geophys. Res. Lett.* 37, L09605. doi: 10.1029/2010GL043227
- Blondeau-Patissier, D., Gower, J. F. R., Dekker, A. G., Phinn, S. R., and Brando, V. E. (2014). A review of ocean color remote sensing methods and statistical techniques for the detection, mapping and analysis of phytoplankton blooms in coastal and open oceans. *Prog. Oceanogr.* 123, 123–144. doi: 10.1016/j.pocean.2013.12.008
- Brando, V. E., Sammartino, M., Colella, S., Bracaglia, M., Di Cicco, A., D'Alimonte, D., et al. (2021). Phytoplankton bloom dynamics in the baltic sea using a consistently reprocessed time series of multi-sensor reflectance and novel chlorophyll-a retrievals. *Remote Sens.* 13, 3071. doi: 10.3390/rs13163071
- Brewin, R. J., Sathyendranath, S., Müller, D., Brockmann, C., Deschamps, P. Y., Devred, E., et al. (2015). The Ocean Colour Climate Change Initiative: III. A round-robin comparison on in-water bio-optical algorithms. *Remote Sens. Environ.* 162, 271–294. doi: 10.1016/j.rse.2013.09.016
- Brockmann, C., Doerffer, R., Peters, M., Stelzer, K., Embacher, S., and Ruescas, A. (2016). "Evolution of the C2RCC neural network for sentinel 2 and 3 for the retrieval of ocean colour products in normal and extreme optically complex waters," in *Proc. Living Planet Symposium*. 740, 1–13. (Prague, Czech Republic: ESA).
- Cazzaniga, I., Zibordi, G., Mélin, F., Kwiatkowska, E., Talone, M., Dessailly, D., et al. (2022). Evaluation of OLCI neural network radiometric water products. *IEEE Trans. Geosci. Remote Sens.* 19 (1-5), 1503405. doi: 10.1109/LGRS.2021.3136291
- Concha, J., Bracaglia, M., and Brando, V. (2021). Assessing the influence of different validation protocols on Ocean Colour match-up analyses. *Remote Sens. Environ.* 259, 112415. doi: 10.1016/j.rse.2021.112415
- D'Alimonte, D., Kajiyama, T., and Saptawijaya, A. (2016). Ocean color remote sensing of atypical marine optical cases. *IEEE Trans. Geosci. Remote Sens.* 54, 6574–6586. doi: 10.1109/TGRS.2016.2587106
- D'Alimonte, D., Zibordi, G., Berthon, J.-F., Canuti, E., and Kajiyama, T. (2011). *Bio-optical algorithms for european seas: performance and applicability of neural-net inversion schemes* (Luxembourg: Publications Office of the European Union).
- D'Alimonte, D., Zibordi, G., Kajiyama, T., and Berthon, J.-F. (2014). Comparison between MERIS and Regional High-Level Products in European Seas. *Remote Sens. Environ.* 140, 378–395.

resolution produced using the OC-CCI processor within the Ocean Colour Thematic Assembly Centre activities. The AERONET Team is acknowledged for the continuous effort in supporting the AERONET-OC subnetwork. Giuseppe Zibordi, Barbara Bulgarelli, and Frederic Melin from the Joint Research Center of the European Commission are acknowledged for establishing and maintaining the Irbe Lighthouse, Gustav Dalen Tower, and Helsinki Lighthouse AERONET-OC sites. ICES and HELCOM along with all single contributors are thanked for the COMBINE *in-situ* dataset. Scientists and technical personnel at SYKE are thanked for the acquisition of the Alg@line *in-situ* dataset. The ESA Sentinel Application Platform and Sentinel tool-box development teams are thanked for making the SNAP software freely available. We are grateful to Vega Forneris and Flavio Lapadula for maintaining the satellite data processing and the satellite data archive at CNR-ISMAR.

Conflict of interest

The authors declare that the research was conducted in the absence of any commercial or financial relationships that could be construed as a potential conflict of interest.

Publisher's note

All claims expressed in this article are solely those of the authors and do not necessarily represent those of their affiliated organizations, or those of the publisher, the editors and the reviewers. Any product that may be evaluated in this article, or claim that may be made by its manufacturer, is not guaranteed or endorsed by the publisher.

- Darecki, M., and Stramski, D. (2004). An evaluation of MODIS and seaWiFS bio-optical algorithms in the baltic sea. *Remote Sens. Environ.* 89, 326–350. doi: 10.1016/j.rse.2003.10.012
- Doerffer, R., and Schiller, H. (2007). The MERIS Case 2 water algorithm. *Int. J. Remote Sens.* 28, 517–535. doi: 10.1080/01431160600821127
- EUMETSAT (2019) *EUMETSAT OCDB user manual. Copyright 2019, copernicus revision 763d8907* (Accessed December 11, 2023).
- EUMETSAT (2021) *Sentinel-3 OLCI L2 report for baseline collection OL_L2M_003 - EUM/RSP/REP/21/1211386* (Accessed December 11, 2023).
- EUMETSAT (2022) *Recommendations for Sentinel-3 OLCI Ocean Colour product validations in comparison with in situ measurements - Matchup Protocols* (Accessed December 11, 2023).
- Finni, T., Kononen, K., Olsonen, R., and Wallström, K. (2001). The history of cyanobacterial blooms in the Baltic Sea. *Ambio* 30, 172–178. doi: 10.1579/0044-7447-30.4.172
- Fleming, V., and Kaitala, S. (2006). Phytoplankton spring bloom intensity index for the baltic sea estimated for the years 1992 to 2004. *Hydrobiologia* 554, 57–65. doi: 10.1007/s10750-005-1006-7
- Fleming-Lehtinen, V., Andersen, J. H., Carstensen, J., Łysiak-Pastuszek, E., Murray, C., Pyhälä, M., et al. (2015). Recent developments in assessment methodology reveal that the Baltic Sea eutrophication problem is expanding. *Ecol. Indic.* 48, 380–388. doi: 10.1016/j.ecolind.2014.08.022
- González Vilas, L., Brando, V. E., Concha, A. J., Dogliotti, A. I., Goyens, C., and Doxaran, D. (2023) *HYPERNETS multi-mission validation of water products V2. Deliverable D7.3, version 1.0, 24/04/2023* (Accessed December 11, 2023).
- González Vilas, L., Brando, V. E., Concha, A. J., Goyens, C., Dogliotti, A. I., Doxaran, D., et al. (2024). Validation of satellite water products based on Hypernets in situ data using a Match-up Database File (MDB) structure. *Front. Remote Sens.*
- Groom, S., Sathyendranath, S., Ban, Y., Bernard, S., Brewi, R., Brotas, V., et al. (2019). Satellite ocean colour: current status and future perspective. *Front. Mar. Sci.* 6, 485. doi: 10.3389/fmars.2019.00485
- Heiskanen, A.-S., Bonsdorff, E., and Joas, M. (2019). “Baltic sea: A recovering future from decades of eutrophication,” in *Coasts and estuaries* (Amsterdam, The Netherlands: Elsevier), 343–362.
- HELCOM (2007). *HELCOM baltic sea action plan* (Helsinki, Finland: HELCOM).
- HELCOM (2017). *Manual for marine monitoring in the COMBINE programme of HELCOM* (Helsinki, Finland: HELCOM).
- HELCOM (2018). *State of the baltic sea—Second HELCOM holistic assessment 2011–2016* (Helsinki, Finland: HELCOM).
- HELCOM (2019). *HELCOM guidelines for monitoring of chlorophyll a* (Helsinki, Finland: HELCOM).
- Hieronimi, M., Müller, D., and Doerffer, R. (2017). The OLCI neural network swarm (ONNS): A bio-geo-optical algorithm for open ocean and coastal waters. *Front. Mar. Sci.* 4, 140. doi: 10.3389/fmars.2017.00140
- Hjerne, O., Hajdu, S., Larsson, U., Downing, A. S., and Winder, M. (2019). Climate driven changes in timing, composition and magnitude of the Baltic Sea Phytoplankton Spring Bloom. *Front. Mar. Sci.* 6. doi: 10.3389/fmars.2019.00482
- Kahru, M., Elmgren, R., Di Lorenzo, E., and Savchuk, O. (2018). Unexplained interannual oscillations of cyanobacterial blooms in the Baltic Sea. *Sci. Rep.* 8, 6365. doi: 10.1038/s41598-018-24829-7
- Kahru, M., Horstmann, U., and Rud, O. (1994). Satellite detection of increased cyanobacteria blooms in the Baltic Sea: Natural fluctuation or ecosystem change? *Ambio* 23, 469–472.
- Kahru, M., Savchuk, O., and Elmgren, R. (2007). Satellite measurements of cyanobacterial bloom frequency in the Baltic Sea: Interannual and spatial variability. *Mar. Ecol. Prog. Ser.* 343, 15–23. doi: 10.3354/meps06943
- Kaitala, S., Zibordi, G., Melin, F., Seppälä, J., and Ylöstalo, P. (2008). Coastal water monitoring and remote sensing products validation using ferrybox and above-water radiometric measurements. *EARSeL eProceedings* 7, 75–80.
- Kajiyama, T., D’Alimonte, D., and Zibordi, G. (2019). Algorithms merging for the determination of chlorophyll-a concentration in the black sea. *IEEE Geosci. Remote Sens. Lett.* 16, 677–681. doi: 10.1109/LGRS.2018.2883539
- Kratzer, S., and Moore, G. (2018). Inherent optical properties of the Baltic Sea in comparison to other seas and oceans. *Remote Sens.* 10, 418. doi: 10.3390/rs10030418
- Kratzer, S., and Vinterhav, C. (2010). Improvement of MERIS level 2 products in baltic sea coastal areas by applying the improved contrast between ocean and land processor (ICOL)—Data analysis and validation. *Oceanologia* 52, 211–236. doi: 10.5697/oc.52-2.211
- Kyryliuk, D., and Kratzer, S. (2019). Evaluation of sentinel-3A OLCI products derived using the case-2 regional coast colour processor over the baltic sea. *Sensors* 19, 3609. doi: 10.3390/s19163609
- Lee, Z., Carder, K. L., and Arnone, R. A. (2014). *Update of the quasi-analytical algorithm (QAA_V6)* (Dartmouth, Canada: IOCCG).
- Leppäranta, M., and Myrberg, K. (2009). *Physical oceanography of the baltic sea* (Berlin/Heidelberg, Germany: Springer).
- Le Traon, P. Y., Reppucci, A., Alvarez Fanjul, E., Aouf, L., Behrens, A., Belmonte, M., et al. (2019). From observation to information and users: the copernicus marine service perspective. *Front. Mar. Sci.* 6, 234. doi: 10.3389/fmars.2019.00234
- Ligi, M., Kutser, T., Kallio, K., Attila, J., Koponen, S., Paavel, B., et al. (2017). Testing the performance of empirical remote sensing algorithms in the Baltic Sea waters with modelled and in situ reflectance data. *Oceanologia* 59, 57–68. doi: 10.1016/j.oceano.2016.08.002
- Mélin, F., and Sclap, G. (2015). Band shifting for ocean color multi-spectral reflectance data. *Opt. Express* 23, 2262. doi: 10.1364/OE.23.002262
- OC-CCI (2022) *Ocean colour climate change initiative (OC-CCI) - phase3. Product user guide for v6.0 dataset* (Accessed December 11, 2023).
- OCEANCOLOUR_BAL_BGC_L3_MY_009_133 (2023) *E.U. Copernicus marine service information (CMEMS). Marine data store (MDS)* (Accessed July 10, 2023).
- OCEANCOLOUR_BAL_BGC_L3_NRT_009_131 (2023) *Marine data store (MDS)* (Accessed July 10, 2023).
- Odermatt, D., Gitelson, A., Brando, V. E., and Schaeppman, M. (2012). Review of constituent retrieval in optically deep and complex waters from satellite imagery. *Remote Sens. Environ.* 118, 116–126. doi: 10.1016/j.rse.2011.11.013
- Omstedt, A., Elken, J., Lehmann, A., and Piechura, J. (2004). Knowledge of the Baltic Sea physics gained during the BALTEX and related programmes. *Prog. Oceanogr.* 63, 1–28. doi: 10.1016/j.pocan.2004.09.001
- O’Reilly, J. E., and Werdell, P. J. (2019). Chlorophyll algorithms for ocean color sensors—OC4, OC5 & OC6. *Remote Sens. Environ.* 229, 32–47. doi: 10.1016/j.rse.2019.04.021
- Pitarch, J., Volpe, G., Colella, S., Krasemann, H., and Santoleri, R. (2016). Remote sensing of chlorophyll in the baltic sea at basin scale from 1997 to 2012 using merged multi-sensor data. *Ocean Sci.* 12, 379–389. doi: 10.5194/os-12-379-2016
- Qin, P., Simis, S. G. H., and Tilstone, G. H. (2017). Radiometric validation of atmospheric correction for MERIS in the Baltic Sea based on continuous observations from ships and AERONET-OC. *Remote Sens. Environ.* 200, 263–280. doi: 10.1016/j.rse.2017.08.024
- Sathyendranath, S., Brewin, R., Brockmann, C., Brotas, V., Calton, B., Chuprin, A., et al. (2019). An ocean-colour time series for use in climate studies: The experience of the ocean-colour climate change initiative (OC-CCI). *Sensors* 19, 4285. doi: 10.3390/s19194285
- Sathyendranath, S., Groom, S. B., Jackson, T., Volpe, G., and Calton, B. (2022). *ESA Ocean colour climate change initiative-phase 3 climate assessment report* (Accessed December 11, 2023).
- Schroeder, T., Behnert, I., Schaale, M., Fischer, J., and Doerffer, R. (2007). Atmospheric correction algorithm for MERIS above case-2 waters. *Int. J. Remote Sens.* 28, 1469–1486. doi: 10.1080/01431160600962574
- Schroeder, T., Fischer, J., Schaale, M., and Fell, F. (2003). “Artificial-neural-network-based atmospheric correction algorithm: application to MERIS data,” in *Proc. SPIE 4892, Ocean Remote Sensing and Applications*. doi: 10.1117/12.467293
- Schroeder, T., Schaale, M., Lovell, J., and Blondeau-Patissier, D. (2022). An ensemble neural network atmospheric correction for Sentinel-3 OLCI over coastal waters providing inherent model uncertainty estimation and sensor noise propagation. *Remote Sens. Environ.* (SPIE) 270, 112848. doi: 10.1016/j.rse.2021.112848
- Simis, S. G. H., and Olsson, J. (2013). Unattended processing of shipborne hyperspectral reflectance measurements. *Remote Sens. Environ.* 135, 202–212. doi: 10.1016/j.rse.2013.04.001
- Simis, S., Qin, P., Attila, J., Kervinen, M., Kallio, K., Koponen, S., et al. (2021). *Baltic sea shipborne hyperspectral reflectance data from 2016 (1.0)* (Zenodo), 5572537.
- Simis, S. G. H., Ylöstalo, P., Kallio, K. Y., Spilling, K., and Kutser, T. (2017). Contrasting seasonality in optical-biogeochemical properties of the Baltic Sea. *PLoS One* 12, e0173357. doi: 10.1371/journal.pone.0173357
- Steinmetz, F., Deschamps, P.-Y., and Ramon, D. (2011). Atmospheric correction in presence of sun glint: application to MERIS. *Opt. Express* (SPIE) 19, 9783–9800. doi: 10.1364/OE.19.009783
- Steinmetz, F., and Ramon, D. (2018). “Sentinel-2 MSI and Sentinel-3 OLCI consistent ocean colour products using POLYMER,” in *Proceedings of the remote sensing of the open and coastal ocean and inland waters* (Honolulu, HI, USA).
- Tilstone, G. H., Pardo, S., Simis, S. G. H., Qin, P., Selmes, N., Dessailly, D., et al. (2022). Consistency between satellite ocean colour products under high coloured dissolved organic matter absorption in the baltic sea. *Remote Sens.* 14 (1), 89. doi: 10.3390/rs14010089
- Toming, K., Kutser, T., Uiboupin, R., Arikas, A., Vahter, K., and Paavel, B. (2017). Mapping water quality parameters with sentinel-3 ocean and land colour instrument imagery in the baltic sea. *Remote Sens.* 9, 1070. doi: 10.3390/rs9101070
- von Schuckmann, K., Le Traon, P.-Y., Smith, N., Pascual, A., Djavidnia, S., Brasseur, P., et al. (2022). Copernicus ocean state report, issue 6. *J. Oper. Oceanogr.* 15, s1–s220. doi: 10.1080/1755876X.2022.2095169
- Warren, M. A., Simis, S. G. H., Martínez-Vicente, V., Poser, K., Bresciani, M., Alikas, K., et al. (2019). Assessment of atmospheric correction algorithms for the sentinel-2A multispectral imager over coastal and inland waters. *Remote Sens. Environ.* 225, 267–289. doi: 10.1016/j.rse.2019.03.018
- Wasmund, N., Tuimala, J., Suikkanen, S., Vandepitte, L., and Kraberg, A. (2011). Long-term trends in phytoplankton composition in the western and central Baltic Sea. *J. Mar. Syst.* 87 (2), 145–159. doi: 10.1016/j.jmarsys.2011.03.010
- Ylöstalo, P., Seppälä, J., Kaitala, S., Maunula, P., and Simis, S. (2016). Loadings of dissolved organic matter and nutrients from the Neva River into the Gulf of Finland—

Biogeochemical composition and spatial distribution within the salinity gradient. *Mar. Chem.* 186, 58–71. doi: 10.1016/j.marchem.2016.07.004

Zhang, D., Lavender, S., Muller, J.-P., Walton, D., Zou, X., and Shi, F. (2018). MERIS observations of phytoplankton phenology in the Baltic Sea. *Sci. Total. Environ.* 642, 447–462. doi: 10.1016/j.scitotenv.2018.06.019

Zibordi, G., Berthon, J.-F., Mélin, F., and D'Alimonte, D. (2011). Cross-site consistent in situ measurements for satellite ocean color applications: the bioMaP radiometric dataset. *Remote Sens. Environ.* 115, 2104–2115. doi: 10.1016/j.rse.2011.04.013

Zibordi, G., Kwiatkowska, E., Mélin, F., Talone, M., Cazzaniga, I., Dessailly, D., et al. (2022). Assessment of OLCI-A and OLCI-B radiometric data products across European seas. *Remote Sens. Environ.* 272, 112911. doi: 10.1016/j.rse.2022.112911

Zibordi, G., Melin, F., and Berthon, J.-F. (2018). A regional assessment of OLCI data products. *IEEE Geosci. Remote Sens. Lett.* 15, 1490–1494. doi: 10.1109/LGRS.2018.2849329

Zibordi, G., Mélin, F., Berthon, J.-F., Holben, B., Slutsker, I., Giles, D., et al. (2009). AERONET-OC: A network for the validation of ocean color primary products. *J. Atmos. Oceanic Technol.* 26, 1634–1651. doi: 10.1175/2009JTECHO654.1